

## KINEMATIC AND CHEMICAL CONSTRAINTS ON THE FORMATION OF M31'S INNER AND OUTER HALO<sup>†</sup>

ANDREAS KOCH<sup>1</sup>, R. MICHAEL RICH<sup>1</sup>, DAVID B. REITZEL<sup>1</sup>, NICOLAS F. MARTIN<sup>2</sup>, RODRIGO A. IBATA<sup>3</sup>, SCOTT C. CHAPMAN<sup>4</sup>, STEVEN R. MAJEWSKI<sup>5</sup>, MASAO MORI<sup>6</sup>, YEONG-SHANG LOH<sup>1</sup>, JAMES C. OSTHEIMER<sup>5</sup>, AND MIKITO TANAKA<sup>7</sup>

*Accepted to the Astrophysical Journal*

### ABSTRACT

The halo of M31 shows a wealth of substructures, some of which are consistent with the assembly from satellite accretion. Here we report on kinematic and abundance results from Keck/DEIMOS spectroscopy in the near-infrared calcium triplet region of over 3500 red giant star candidates along the minor axis and in off-axis spheroidal fields of M31. These data reach out to large radial distances of about 160 kpc. The derived radial velocity distributions show an indication of a kinematically cold substructure around  $\sim 17$  kpc, which has been reported before. We devise a new improved method to measure spectroscopic metallicities from the calcium triplet in low signal-to-noise spectra using a weighted coaddition of the individual lines. The resulting distribution (accurate to  $\sim 0.3$  dex down to signal to noise ratios of 5) leads us to note an even stronger gradient in the abundance distribution along M31's minor axis and in particular towards the outer halo fields than previously detected. The mean metallicity in the outer fields reaches below  $-2$  dex, with individual values as low as  $\lesssim -2.6$  dex. This is the first time such a metal poor halo has been detected in M31. In the fields towards the inner spheroid we find a sharp decline of  $\sim 0.5$  dex in metallicity in a region at  $\sim 20$  kpc, which roughly coincides with the edge of an extended disk, previously detected from star count maps. A large fraction of red giants that we detect in the most distant fields are likely members of M33's overlapping halo. A comparison of our velocities with those predicted by new N-body simulations argues that the event responsible for the giant Stream is most likely not responsible for the full population of the inner halo. We show further that the abundance distribution of the Stream is different from that of the inner halo, from which it becomes evident, in turn, that the merger event that formed the Stream and the outer halo cannot have contributed any significant material to the inner spheroid. All these severe structure changes in the halo suggest a high degree of infall and stochastic abundance accretion governing the build-up of M31's inner and outer halo.

*Subject headings:* Galaxies: abundances — Galaxies: evolution — Galaxies: kinematics — Galaxies: structure — Galaxies: stellar content — Galaxies: structure — Galaxies: individual (M31)

### 1. INTRODUCTION

With the discovery of the Giant Stream (Ibata et al. 2001), the mapping of complex structures in the “halo” of M31 (Ferguson et al. 2002; Gilbert et al. 2007; Ibata et al. 2007), and the isolation of an extended kinematic disk structure (Ibata et al. 2005) the idea that the radially more distant populations of M31 originate in accretion events has become established. Even a subset of M31 satellites might relate to the breakup of a mas-

sive progenitor, based on the polar and planar alignment of a number of its early-type satellite galaxies (Koch & Grebel 2006).

Prior to this paradigm shift in the description of the M31 halo, relatively shallow Hubble Space Telescope (HST) imagery revealed what appeared to be a mostly metal rich M31 halo (e.g. Rich et al. 1996; Bellazini et al. 2003). Mould & Kristian (1986) were the first to find a metal rich (47 Tuc-like) halo population, using ground-based imaging. The widespread presence of this metal rich population as well as the descending red giant branch (RGB; in contrast to the metal poor globular clusters) was noted by Bellazini et al. (2003). Ground-based minor axis star counts appear to show a smooth  $r^{1/4}$  spheroid (Pritchett & van den Bergh 1994), and some studies have argued that the metal rich halo population is an extension of the metal rich bulge (e.g. Mould & Kristian 1986; Guhathakurta et al. 2006). But alternatively, the case has been made that the metal rich stars more closely coincide with the perturbed regions (Ferguson et al. 2002).

Metal poor stars around M31 were already indicated in photometric studies of its halo at projected distances of 7 kpc (Mould & Kristian 1986) to 20 kpc (Durrell 2001). Subsequent spectroscopic surveys then fully re-

Electronic address: akoch@astro.ucla.edu

<sup>†</sup> Some of the data presented herein were obtained at the W.M. Keck Observatory, which is operated as a scientific partnership among the California Institute of Technology, the University of California and the National Aeronautics and Space Administration. The Observatory was made possible by the generous financial support of the W.M. Keck Foundation.

<sup>1</sup> UCLA, Department of Physics and Astronomy, Los Angeles, CA, USA

<sup>2</sup> Max Planck Institute for Astronomy, D-69117 Heidelberg, Germany

<sup>3</sup> Observatoire de Strasbourg, F-67000 Strasbourg, France

<sup>4</sup> Institute of Astronomy, Cambridge University, Cambridge, UK

<sup>5</sup> Department of Astronomy, University of Virginia, Charlottesville, VA, USA

<sup>6</sup> Center for Computational Sciences, University of Tsukuba, Tsukuba, Ibaraki 305-8577, Japan

<sup>7</sup> National Astronomical Observatory of Japan, 2-21-1 Osawa, Mitaka, Tokyo 181-8588, Japan

vealed a complex picture of the halo composition: Using the well-established near-infrared calcium triplet (CaT) as a metallicity indicator, Reitzel & Guhathakurta (2002) find metal poor stars at 19 kpc on the minor axis. Benefitting from much larger samples, Chapman et al. (2006) and Kalirai et al. (2006a) argue based on kinematics and metallicity that the expected metal poor halo population is in fact present. Giants with the radial velocity of M31 are claimed as members of the halo to distances in excess of 100 kpc (Ostheimer 2003; Gilbert et al. 2006) and an overall metallicity gradient of the M31 halo is proposed by Kalirai et al. (2006a). Yet, over much of this region, Ibata et al. (2007) find clear evidence of density enhancements associated with accretion. What fraction of the outer halo is then comprised of such recently accreted material? In particular the chemical composition of the outer stars remains unknown, and depending on the adopted  $[\alpha/\text{Fe}]$  ratio, Kalirai et al. (2006a) estimate a mean metallicity in the outermost field  $\sim 0.3$  dex higher than the mean Milky Way metallicity (for Solar scaled abundances), or a mean that is comparable to the Milky Way halo under the assumption of strong  $\alpha$ -enhancement.

In fact, pencil beam ultradeep imaging using the Advanced Camera for Surveys (ACS) on board the HST, offers a complementary picture of the complexity present in the halo populations. The placement of these deep imaging fields has benefitted from the starcount maps and Keck/DEIMOS kinematic studies. Brown et al. (2003) first demonstrated that a minor axis field projected at 11 kpc contains an indisputable range in age and abundance, extending to nearly-Solar, and a predominant age range from 6–10 Gyr. Comparing 3 fields, in the inner spheroid (at 11 kpc), the M31 disk and on the Ibata et al. (2001) debris stream, Brown et al. (2006) find the disk to be younger and more metal rich, and lacking old stars. They find the stream and spheroid fields to be indistinguishable based on their color-magnitude diagrams (CMDs), leading to the conclusion that only one progenitor is responsible for the debris field in the inner halo region. However, if dynamical mixing were efficient in these regions, it could also erase the signatures from different sources. Brown et al. (2007) investigate a field at 21 kpc and find evidence that its population is marginally older and more metal poor than the inner halo field.

The present-day pencil beam surveys have found clear evidence of an age range in every field studied and appear to support other evidence of a gradient in age and abundance. What has been lacking to date has been a survey of abundances and kinematics that ties these fields together and provides a context for the interpretation of these deep fields. This is one aim of this paper, and a natural extension of our systematic survey of the structure and kinematics of M31 along its southwest minor axis.

While it is attractive to seek *one* massive progenitor for the inner debris field there are several arguments against this position. First, the existence of both the giant stream and the extended disk suggest at least two very different sources for the debris field at 11 kpc. Second, the dramatic variation of the extended spatial structure of the debris field as a function of metallicity and age (Ferguson et al. 2002) is best understood by invoking multiple events involving different accretors. More-

over, the distant rotating disk-like population (Ibata et al. 2005) is superposed on other, likely unrelated, structures that are suggestive of shells associated with the giant Stream merger (see also Ibata et al. 2007). It is then an intriguing question, whether a corresponding measurable abundance change occurs at the point where this field ends.

In the context of CDM models (e.g. Bullock & Johnston 2005) halos are thought, in general, to accrete from the debris of lower mass satellites. Yet Mouhcine et al. (2005) find a correlation between parent galaxy luminosity and halo metallicity. Nominally, M31 has a high metallicity halo and falls in this relationship alongside galaxies with more prominent bulges. There is a paradox: how can the halo of M31 be dominated by stochastic accretion events, yet still have an  $r^{1/4}$  profile and still appear to follow trends set by luminosities of the host galaxies?

We report here the culmination of an observational campaign begun in 2002; Table 1 lists the observing run details by Principal Investigator. This Paper is organized as follows: In §2 we present our observations and the standard reduction steps taken, while §3 describes our radial velocity measurements. The dwarf/giant separation is discussed in §4 and in §5 we devise a new technique to measure spectroscopic metallicities from the CaT. The following sections are then dedicated to the analysis of kinematic (§6) and abundance (§7) substructures and gradients in M31’s halo. Finally, §8 summarizes our findings.

## 2. OBSERVATIONS AND REDUCTION

In the course of an ongoing large Keck program (PI: R. M. Rich) that aims at elucidating the formation history of M31’s halo structures based on the kinematics and chemical analyses of red giants, we collected a vast spectroscopic data set, which covers, amongst others, fields on the minor axis of M31 reaching from 9 kpc out to large projected distances of  $\sim 160$  kpc towards the southeast<sup>9</sup>. These fields were originally imaged by Ostheimer (2003). Two additional fields at 60 kpc on the minor axis were obtained in the course of a large DEIMOS survey covering a wide set of fields spread across M31’s full halo and disk components (PI: S. Chapman; see Chapman et al. 2006). In this Paper, we will focus on the analysis of the minor axis data and those off-axis fields in the southeast halo quadrant, while the fields located on top of the Giant Stellar Stream (Ibata et al. 2001), and those coinciding with the HST fields of Brown et al. (2003; 2006; 2007) will be the subject of a series of forthcoming papers. For details on the overall target selection, observation strategy and data collection for the whole project we refer the reader to Kalirai et al. (2006a,b) and Gilbert et al. (2006, 2007).

### 2.1. Observations

Observations were carried out using the DEIMOS multislit spectrograph at the KeckII 10 m telescope over a number of observing runs from 2002 through 2006 (Table 1), using a slit width of  $1''$ . We used the 1200 line  $\text{mm}^{-1}$  grating, which gives a dispersion of  $0.33 \text{ \AA pixel}^{-1}$

<sup>9</sup> Throughout this work we will adopt a distance to M31 of 784 kpc (Stanek & Garnavich 1998)

and a spectral resolution of  $1.41\text{\AA}$ , as estimated from the width of the sky lines. The majority of the spectra were centered at a wavelength of  $7800\text{\AA}$ , yielding a full spectral coverage of  $\sim 6500\text{--}9200\text{\AA}$ , which comprises the dominant near infrared lines of the CaT around  $8500\text{\AA}$ . Typical integration times were 1 hour per mask, while setup f109.1 (at 9 kpc) was exposed for 3 hours in total. Fig. 1 shows the location of the slit masks discussed in this paper on an INT based star count map (M. Irwin, private communication; Ibata et al. 2007). Details on these masks are given in Table 1.

### 2.2. Data reduction

Reduction of the spectra was performed with the *spec2d* pipeline, which has been designed at the University of California, Berkeley for the DEEP2 survey<sup>10</sup>. The standard reduction steps comprise flat fielding, wavelength calibration via arc lamp spectra and sky spectrum removal. The total number of extracted science spectra<sup>11</sup> finally amounts to 3631 (see Table 2), where the signal to noise ( $S/N$ ) ratios typically range from 2 to 60 per pixel (although a handful of the brightest foreground dwarf spectra reach as high as  $\sim 120$ ) with a median of 8.5. Fig. 2 displays a number of sample spectra of both high and low  $S/N$  around the CaT and the sodium doublet region, which we will utilize to separate M31 giants from foreground dwarfs in Section 4.

### 2.3. Photometry

The photometry of our targets, which will be required later on to perform a color-based foreground separation and to calibrate our spectroscopic metallicity measurements, was taken from two sources: For the fields targeted in the outer regions of M31's halo ( $R \gtrsim 25$  kpc) we used the Washington  $M$ ,  $DDO51$  and  $T_2$  photometry of Ostheimer (2003), which provides a strong separation criterion for red giant selection (Palma et al. 2003). These filters were transformed from the Washington system into standard Johnson-Cousins  $V$  and  $I$  magnitudes by applying eqs. 1,2 of Majewski (2000).

The photometry of targets in our inner fields ( $R \lesssim 25$  kpc) on M31's minor axis was, on the other hand, taken from the MegaCam/Megapipe archive (Gwyn 2008). These data are available in  $i'$  and either  $g'$  or  $r'$ . Typical exposure times range from 800 to 3757 s for  $i'$ , 1600 to 3200 s for  $r'$  and 1445 to 3468 s for  $g'$ . Photometric errors in the catalog are below 0.1 mag for  $g' < 24$  mag, and rise to 0.25 mag at  $g = 26$  mag. The errors in  $r'$  are well below 0.1 mag for  $r' < 24$  mag and reach 0.2 mag at  $r' = 25$  mag. Finally, errors on the  $i'$ -band magnitudes are below 0.1 mag for almost the entire sample below 22.5 mag, with a maximum error of 0.15 mag at  $i' = 24$  mag. The photometric data was then matched to our spectroscopic catalog by requiring the coordinates from the two sets to match within better than  $1''$ . In most cases, the match was better than  $0.2''$ .

In order to determine the spectroscopic metallicity of each star,  $V$ -band magnitudes in the Johnson-Cousins system are required. As only the  $g'$  or  $r'$  and  $i'$  filters

in the photometric system of the CFHT are available, a transformation to  $V$  magnitudes is determined from the latest Padova stellar isochrones (Marigo et al. 2008), which are available in the CFHT photometric system as well as for Johnson  $V$ . In practice, we obtained transformations from isochrones with metallicities ranging from  $-2.3$  to  $+0.18$  dex and ages of 10 and 12 Gyr. The transformation from  $g', i'$  to  $V$  was obtained in four sections:

$$\begin{aligned} V &= g' + 0.39(g' - i') + 0.010; & g' - i' < 1.25 \\ V &= g' - 0.34(g' - i') - 0.050; & 1.25 \leq g' - i' < 1.70 \\ V &= g' - 0.06(g' - i') - 0.525; & 1.70 \leq g' - i' < 3.85 \\ V &= g' - 0.22(g' - i') + 0.740; & 3.85 \leq g' - i' \end{aligned} \quad (1)$$

On the other hand, the transformation from  $r', i'$  to  $V$  is defined as follows:

$$\begin{aligned} V &= r' + 0.98(r' - i') + 0.048; & r' - i' < 1.8 \\ V &= r' + 0.19(r' - i') + 0.445; & 1.8 \leq r' - i' < 4.0 \\ V &= r' + 1.03(r' - i') - 1.500; & 4.0 \leq r' - i' \end{aligned} \quad (2)$$

Typically, these equations are insensitive to the adopted metallicity and age of the isochrones and differences in  $V$ -magnitude from the different isochrones are less than 0.05 mag. Only for the super-solar isochrone, the overall systematic errors increase to 0.1 mag. To account for this we add a 0.1 mag uncertainty in quadrature to the final error estimates on the  $V$ -band magnitude.

The resultant CMDs for all targeted objects are shown in Fig. 3, separately for M31 giant candidates, foreground dwarfs and contaminating background galaxies that were separated using the methods outlined in Sect. 4.

## 3. VELOCITY MEASUREMENTS

Radial velocities were measured by cross correlating our DEIMOS spectra against a high  $S/N$  template spectrum of the bright K1 red giant HD139195, which was observed using the same instrumental setup as our observations (M. Geha, private communication; Simon & Geha 2007). In this way we avoid any systematic uncertainties occurring from potentially different spectral resolutions and dispersions. The correlation was performed using IRAF's<sup>12</sup> *fxcor* task. Preferentially, the entire covered spectral region was used in the correlation, where we rejected the wavelength regions of telluric absorption, in particular the prominent atmospheric A- and B-bands at  $\lambda\lambda 7600, 6860\text{\AA}$ . For cases in which the correlation of the entire spectrum produced weak or no correlation peaks, i.e., for the lowest  $S/N$  spectra, we restricted the windows to single narrow regions around prominent absorption features, such as the CaT from  $8475\text{--}8662\text{\AA}$  and/or the Na doublet from  $8179\text{--}8200\text{\AA}$ . Choice of these band passes will minimize the contribution of potential residual telluric absorption lines (e.g., Schiavon et al. 1997).

Each correlation peak was examined by eye to avoid spurious detections, which might lead to significantly erroneous velocity estimates. A Gaussian fit to the strongest correlation peak then yielded the final relative radial velocity value for the respective spectrum. Finally,

<sup>10</sup> [http://astron.berkeley.edu/~sim\\$cooper/deep/spec1d/primer.html](http://astron.berkeley.edu/~sim$cooper/deep/spec1d/primer.html)

<sup>11</sup> The pipeline also extracts additional point sources that serendipitously fell on the slit during the exposures. These objects are not considered in the present work.

<sup>12</sup> IRAF is distributed by the National Optical Astronomy Observatories, which are operated by the Association of Universities for Research in Astronomy, Inc., under cooperative agreement with the National Science Foundation.

heliocentric corrections were computed for each star individually to yield heliocentric radial velocities,  $v_{\text{HC}}$ , that we will use for the remainder of this work.

The measurement errors on the radial velocities are returned by *fxcor* and are internally computed based on the Tonry-Davis  $R$ -value (Tonry & Davis 1979) of the cross correlation. Thus our median random velocity error amounts to  $8.0 \text{ km s}^{-1}$ . Due to our interactive procedure of assessing each spectrum by eye, we were able to discard bad spectra and cases in which no correlation peak could be discerned on the spot from our sample. These are not considered for the remainder of this work. Moreover, red background galaxies, which significantly contaminate our target sample (of the order of 11% by numbers), were identified based on their emission and absorption lines and culled from the present sample (see appendix).

A total of 110 stars were observed on adjacent masks. These repeat observations allow us to further assess the accuracy of our velocity measurements. We find an overall good agreement between the independent velocity measurements of the same stars from different masks: the mean deviation is  $0.3 \text{ km s}^{-1}$  and the  $1\sigma$  scatter amounts to  $8.2 \text{ km s}^{-1}$ , which is consistent with our measurement errors. The according reduced  $\chi^2 = 1/N \sum_i \frac{(v_{i,1} - v_{i,2})^2}{(\sigma_{i,1}^2 + \sigma_{i,2}^2)}$  is close to unity. Thus we conclude that our duplicate velocity measurements are consistent within the uncertainties. Moreover, this shows that the formal errors returned by *fxcor* correctly reflect the accuracy of our data, also in the light of potential template-target mismatches in stellar type (e.g., Majewski et al. 2004), so that there is no need to re-scale these values (cf. Koch et al. 2007). As the final velocity for stars with repeat measurements we adopted the error-weighted mean of the individual values. As a result, reliable velocities could be determined for 2262 of our stars (see Table 2).

#### 4. MEMBERSHIP SEPARATION

In order to isolate the true sample of M31 member stars from undesired contamination of numerous foreground Milky Way dwarfs, we utilize the three strongest discriminators, viz.  $V - i'$  color, the equivalent width (EW) of the Na I doublet at  $\lambda\lambda 8189, 8193\text{\AA}$ , and radial velocity. In practice, the EWs of the two Na lines were measured by numerically integrating the spectral flux within a bandpass from  $8179\text{\AA}$  to  $8200\text{\AA}$  with suitable continuum bandpasses (Gilbert et al. 2006), and the errors were obtained by Monte Carlo simulations accounting for the continuum variance of the spectra.

To achieve a separation of dwarfs and giants, we follow Gilbert et al. (2006) in splitting our complete observed data set into one dwarf- and one giant training sample: For this purpose, all stars with radial velocities below  $-200 \text{ km s}^{-1}$  were considered to be M31 red giants, whereas those exceeding  $-50 \text{ km s}^{-1}$  are most likely foreground stars. Since it cannot be assumed *a priori* that the color or Na EW distributions constitute well defined analytical, e.g. Gaussian, profiles, we instead define empirical probability distributions (PDFs)  $P$  from the actual observed training samples in color and Na EW space. The PDFs were then convolved with the individual measurement errors. Likewise, for defining the PDF with respect to radial velocity, we adopted a color cut at  $V - i' = 2.0$ , where stars above this limit are taken to

be dwarf candidates. In parallel, taking advantage of the surface gravity sensitivity of the Na doublet (Schiavon et al. 1997), we flagged stars with EWs above  $2.5\text{\AA}$  as dwarfs. These empirical limits were chosen because they turned out to optimize the separation in the  $V - i'$  vs. Na EW parameter space. For the M31 giant radial velocity distribution, on the other hand, we adopted a one-sided Gaussian centered at a systemic velocity of  $-300 \text{ km s}^{-1}$  with a radial velocity dispersion of  $85 \text{ km s}^{-1}$ , in concordance with the values of M31's outer halo component (e.g., Reitzel & Guhathakurta 2002). All stars with velocities below  $-300 \text{ km s}^{-1}$  were assigned a probability of unity in the giant training sample.

Although the number of dwarf stars in this low-velocity regime is expected to be well below 1% and their contribution to the final velocity histograms may be negligible (Gilbert et al. 2006), we will turn to a detailed treatment of this component in Sect. 4.1.

Fig. 4 shows the resulting PDFs of the training samples as dashed lines. The final probability of any star from our sample, with its set of ( $v_{\text{HC}}, V - i', \text{Na EW}$ ), to be either a dwarf or a giant was then determined from the PDFs, normalized to unity, in each parameter and combining these values into a total probability of being a giant:  $P_{\text{giant}} = P_{\text{giant}}(V - i') \times P_{\text{giant}}(\text{Na EW}) \times P_{\text{giant}}(v_{\text{HC}})$ , and likewise for the probability of being a dwarf. If the resulting logarithmic likelihood  $L = \log(P_{\text{giant}}/P_{\text{dwarf}})$  is less than zero, the star is considered a dwarf, while  $L > 0$  signifies likely giant star candidates (Gilbert et al. 2006). The *a posteriori* histograms in Fig. 4 illustrate our full data set, based on the selection method described above. It is evident that the selected samples in all parameters are fully compatible with the pre-defined simple training samples and that the number of remaining dwarf contaminants in our cleaned M31 giant sample can be expected to be negligible. There is nonetheless a considerable overlap of dwarf and giant stars in color space. Moreover, we note the presence of a population of stars, flagged as dwarfs based on the full likelihood analysis, which exhibit small EWs of the Na doublet. From this it becomes obvious that it is in fact necessary to include the entire set of available information in color, EW and velocity in the analysis to obtain an optimal separation. On the other hand, there will be an inevitable, though small, fraction of interlopers that cannot be reliably detected using the traditional separation criteria, due to potential covariances between each of the parameters. For instance, we note the presence of one star with colors and moderate Na widths representative of a dwarf star (as subsequently verified by its spectral features), but with a high negative velocity of  $-280 \text{ km s}^{-1}$ . In this case, the velocity criterion will override the other discriminators and lead to classifying this star as an M31 member. Such cases could be mainly resolved by visual inspection of the individual spectra.

We also note that we refrain in our dwarf/giant separation from adopting additional secondary parameters such as weaker spectral features (e.g., K I EWs, TiO bands, embedded within telluric absorption bands) to avoid adding further noise to the final PDFs. Furthermore, we did not weight our combined likelihood by the number of available diagnostics to account for potential outliers in either of the parameters, thereby yielding a

statistically more robust and uniform rejection of dwarfs (cf. Gilbert et al. 2006).

To assess the accuracy and efficiency of the separation methods described above, we ran a comprehensive suite of *Monte Carlo simulations*. To this end, each of the three indicators was varied  $10^4$  times by its measurement uncertainty, from which subsequently new PDFs were built and each target’s dwarf/giant status was re-determined. *As a result, 92% of those stars previously classified as giants were still classified as such in 95% ( $2\sigma$ ) of the Monte Carlo realizations. Thus we are convinced to have obtained a solid dwarf/giant separation of our sample. In particular, none of the results obtained in this work changes significantly, whether “all” giants are included or only those with secure,  $2\sigma$ -classifications.* The final number of giant candidates per field is listed in Table 2. The ratio of giant to dwarf stars decreases with increasing radial distance from M31 (Fig. 4, bottom right), as expected as the M31 halo density levels off, until the halo of M33 contributes giants in the outermost fields.

There is still a non-negligible fraction of stars classified as giants present in a transitional region around  $-150 \text{ km s}^{-1}$  ( $\sim 1.7\sigma$  above the systemic velocity), which prevails in the outermost minor axis fields (Sect. 6.2). Another noteworthy outcome of our dwarf removal is that the addition of velocity as a membership criterion effectively deprives the sample of red giants above  $-100 \text{ km s}^{-1}$ . This limit already corresponds to removing stars that deviate by more than approximately  $2.3\sigma$  from the sample, and we do not expect the presence of any major population of M31 stars in this high velocity regime. Considering the limited S/N of the spectra in our dataset as well as that of the photometry, we have concluded that it is essential to use radial velocity as a dwarf/giant separation criterion. As a result, the velocities of our dwarf-cleaned sample span a full range from  $-570$  to  $-100 \text{ km s}^{-1}$ . Additionally, the constancy of the foreground Galactic dwarf sample’s velocity and dispersion (Fig. 11, bottom left) over the entirety of the M31 halo strengthens further our case for efficient dwarf/giant separation.

In a recent work, Sherwin et al. (2008) predicted that a total number of  $\sim 5$  hypervelocity stars with velocities below  $-420 \text{ km s}^{-1}$  should be identifiable in M31’s halo. However, given M31’s large overall velocity dispersion and the low number of stars with the highest negative velocities, it is impossible to resolve, whether any of those stars in our sample are in fact ejected from the center of M31, or if they are canonical ( $2\sigma$ -) members of its genuine halo.

#### 4.1. Comparison with the Besançon model

As Fig. 3 shows, there are still a number of stars present bluewards of the most metal poor isochrone that were classified as M31 giants based on all separators. However, it cannot be excluded that a subset of these may be blue, metal poor Galactic halo dwarfs, which typically have negligible Na doublet lines and a broad range in radial velocities (Fig. 5). Thus these contaminants are indistinguishable from the giant sample and their separation is insoluble based on the canonical membership criteria. It is important to assess the fraction of these blue stars, since their systematically weaker CaT lines

will yield falsified, low metallicities.

To this end, we queried models of the Besançon Galactic foreground population (Robin et al. 2003) using color cuts and spatial locations in analogy to the observed samples. The resulting distribution for the outermost field at 160 kpc is illustrated in Fig. 5 (right panel). We chose to exemplary plot this outermost field, because it is the one for which the Milky Way contamination is expected to be the highest. The first thing to note is that there is in fact a non-zero population of Galactic stars predicted at M31’s systemic velocity, with radial velocities as low as  $-420 \text{ km s}^{-1}$  (although we note that the velocity dispersion in the Galactic model may in fact be overestimated). Most of the contaminants are, however, distinguishable, either by their high velocities or their redder colors. We thus estimate the number of undetectable blue stars in our sample by determining the *predicted fraction of dwarfs* with  $v_{\text{HC}} \lesssim -150 \text{ km s}^{-1}$  and  $V-i' \lesssim 1$  to those dwarf stars in the color-velocity space that we are able to distinguish (Fig. 4; Sect. 4). Multiplying this fraction with the number of our observed giant candidates (Table 2) then shows that there are typically no more than 0–2 blue dwarf stars to be expected per field in our giant sample that cannot separated by any of the observable criteria (see also Fig. 5, right panel), leading to a total predicted number of 35 such contaminants in the entire sample. If present, these will have a negligible effect on the more populous, true giant sample.

Martin et al. (2007) model the CMD of these fields, reaching fainter than the limit of our spectroscopy, and find no evidence for excess star counts of Galactic members. In principle, dwarf members of the Andromeda-Triangulum stream or a potential contaminant may be present, especially in the M31 giant-poor outer fields. Rocha-Pinto et al. (2004) have measured radial velocities of Andromeda-Triangulum stream members, finding one star with  $-245 \text{ km s}^{-1}$ , but with most stars at higher velocity. Furthermore, the Monoceros Ring, whose main sequence stars can overlap with M31 stars near the Tip RGB, have a radial velocity that is high enough (at  $-75 \text{ km s}^{-1}$  with a dispersion of  $26 \text{ km s}^{-1}$ ; Martin et al. 2006a) so that they are not an issue in the analysis. Based on these studies, neither of the systems poses any risk for contaminating the field with stars at the radial velocity of M31.

## 5. A NEW METHOD FOR CALCIUM TRIPLET METALLICITIES

In the frequent cases of low spectral resolution and/or low S/N ratios the last resort is to measure gravity and/or abundance-sensitive indices in band passes a few times the spectral resolution, which are then calibrated theoretically via a grid of synthetic spectra (e.g., Jones et al. 1996). The latter is in general a critical endeavor for the CaT, since these lines are formed in the upper chromospheres of the stars, which ideally requires a full non-local thermodynamic equilibrium treatment (Smith & Drake 1990; Jørgensen et al. 1992). Detailed model computations are however sparse so that present-day studies of stellar populations mostly rely on empirical calibrations (Cenarro et al. 2001; and references therein).

Canonically, the line strength of the near-infrared CaT,  $\Sigma W$ , has been defined by a weighted sum of the three

individual lines' pseudo equivalent widths,  $EW_i$ :

$$\Sigma W = \sum_{i=1}^3 w_i EW_i = \sum_{i=1}^3 w_i \int_{BP_i} \left(1 - \frac{F(\lambda)}{F_{c,i}}\right) d\lambda, \quad (3)$$

where  $F$  denotes the flux in a predefined set of line band passes ( $BP_i$ ) and  $F_c$  is the continuum level as determined in a set of continuum bands. There is no physical motivation to prefer any set of the weight factors  $w_i$  over the other, as long as a consistent definition is used between the target red giants to be calibrated and those in the calibrator systems, i.e., the high  $S/N$  Galactic globular cluster spectra. The choice of the weights is mostly governed by the spectral quality and measurability of each of the Ca lines. In this vein, the most frequently used weights throughout the literature are ( $w_i=1 \forall i$ ; e.g., Armandroff & Zinn 1988), ( $w_1 = 0, w_2 = 1, w_3 = 1$ ; e.g., Armandroff & DaCosta 1991) and ( $w_1 = 0.5, w_2 = 1, w_3 = 0.6$ ; e.g., Rutledge et al. 1997a). The EWs are then either determined by numerically integrating the spectral flux over the full bandpass or by fitting an analytical function  $F(\lambda)$  to the line profile. However, both methods tend to fail at the lowest  $S/N$  ratios, where a pure numerical integration merely reflects the noise of the spectrum rather than the actual EWs, while the lines cannot be reliably fit anymore in the low  $S/N$  regime. Typically, the limiting  $S/N$  for which CaT based  $[\text{Fe}/\text{H}]$  measurements are given in the literature lies at 10–15.

At the low  $S/N$  ratios of our faintest DEIMOS targets, which reach as low as 2–5, a reliable determination of the CaT EWs is not feasible. Moreover, the presence of sky line residuals around the CaT often leads to artificially increased widths if uncritically integrated over the respective band passes. In particular, the third of the CaT lines at 8662Å is susceptible to this increased noise component.

Hence, in order to enhance the  $S/N$  in the CaT of each individual spectrum, we define a coadded line strength  $\langle \Sigma W \rangle$  in that we interchange the order of summation and integration in eq. 3:

$$\langle \Sigma W \rangle = \int_{\langle BP \rangle} \sum_{i=1}^3 w_i \left(1 - \frac{F(\lambda - \lambda_{0,i})}{F_{c,i}}\right) d(\lambda - \lambda_{0,i}). \quad (4)$$

That is, each line center is shifted towards a zero wavelength before performing a weighted coaddition of the three lines in this rest frame, using the identical weight factors as in the canonical definition. Mathematically, this expression is fully equivalent to the traditional definition in eq. 3, but it provides the advantage of integrating the *coadded flux*, resulting in an increased effective  $S/N$ . The integration is then carried out over a single common band pass. This procedure strictly presupposes that the individual band passes  $BP_i$  all have the same width and location relative to the line center so that  $BP_i - \lambda_i$  is the same for each of the lines. However, we will tie our measurements to a metallicity reference scale by using our own suite of measurements in Galactic globular clusters. Thus possible differences in the band passes will affect the reference spectra and our target spectra in the same manner and these will not introduce any systematic bias. In the following, we will follow the prescription of Rutledge et al. (1997a) by adopting the

line weights of 0.5, 1 and 0.6. Our coaddition method will improve the effective  $S/N$  in the CaT region by a factor of  $\sqrt{\sum w_i}$ , or 1.45, so that we will be capable of measuring metallicities even with  $S/N$  as low as  $\sim 7$ –10. Furthermore, the coadded line is more robust against potential sky residuals and noise spikes, enabling us to fit a line profile (see the illustration in Fig. 6). In practice, we fit the resulting line with a Penny function, i.e., a Gaussian plus a Lorentz component, which has proven to provide the best representation of the line wings (Cole et al. 2004).

In order to tie our CaT metallicity measurements in the M31 stars to a reference scale, we performed the identical coaddition technique as described above on a sample of globular clusters of known metallicity and thus derived the CaT line strengths of the globular cluster stars. Since no observations of globular cluster standard stars were taken for the present project using the same instrumental set up as for the M31 science observations, we exploited the data set of Koch et al. (2006), which consists of high  $S/N$  spectra of 80 red giants in four Galactic clusters, NGC 3201, 4590, 4147 and 5904, obtained with the FLAMES spectrograph at ESO/VLT (Pasquini et al. 2002). Since the FLAMES spectrograph provides a higher spectral resolution than DEIMOS, we degraded the spectral resolution of the FLAMES spectra to match that of DEIMOS. The final calibration of the line strengths onto metallicity was then achieved accounting for the stars' magnitude above the horizontal branch (HB; e.g., Rutledge et al. 1997a,b), where we find the following relations

$$W' = \langle \Sigma W \rangle + 0.55 (V - V_{\text{HB}}) \quad (5)$$

$$[\text{Fe}/\text{H}]_{\text{CaT}} = -2.90 + 0.45 W' \quad (6)$$

with an r.m.s. scatter of 0.02 dex on the  $[\text{Fe}/\text{H}]_{\text{CaT}}$  calibration of eq. 6. These relations from the FLAMES data are shown in Fig. 7. In this calibration we explicitly adopted the globular cluster metallicity scale of Carretta & Gratton (1997). Furthermore, we assumed a HB apparent magnitude of 25.17 mag for the M31 stars, which corresponds to the mean magnitude of its halo red HB population (Holland et al. 1996). The extent of M31's halo will inevitably lead to a spread of distances along the sight so that the adoption of a single HB magnitude is a simplifying assumption. Ibata et al. (2007) estimate that, for an extended  $\rho(r) \propto r^{-2.9}$  density profile, the variation in the distance modulus is typically less than 0.5 mag. Translating this into a HB spread and by applying our calibrations (Eqs. 5,6) this leads to an uncertainty of 0.12 dex on the spectroscopic metallicities. Given the *a priori* unknown distance of individual red giants, this source of uncertainty cannot be eliminated and will affect all spectroscopic metallicity measurements in M31. Furthermore, the adoption of the HB of the oldest stars will introduce a systematic effect on spectroscopic  $[\text{Fe}/\text{H}]$  estimates in the presence of a non-negligible intermediate-age population. Koch et al. (2006) estimate that the simplification of a single-age HB results in a bias of the order of  $-0.1$  dex, that is, the intermediate-age stars may be 0.1 dex too metal poor. This is the same order of magnitude that Cole et al. (2004) find from their cluster sample, which includes a number of young open clusters. Of course, one cannot

assess which stars are affected to what extent, since their ages cannot be assigned *a priori*. In this context, we note that also the M31 globular clusters show a mild trend in mean  $M_v(\text{HB})$  vs.  $[\text{Fe}/\text{H}]$ ; this may be lessened by the brighter HBs of intermediate age populations. This trend is 0.4 mag but has a full width of 0.6 mag (Rich et al. 2005, their Fig. 12), with a  $1\sigma$  scatter of 0.2 dex. This compares to a small formal random uncertainty of typically less than 0.01 dex on  $[\text{Fe}/\text{H}]_{\text{CaT}}$  that is introduced by the photometric errors through Eqs. 5,6. Even an unrealistically large error of 1mag on a star's  $V$  magnitude would result in a metallicity error of 0.23 dex.

We note that the coefficients of our relations in Eqs. 5,6 are slightly different from the standard calibration of Rutledge et al. (1997b), but for the sake of consistency between our own measurements and our own suite of calibration clusters, we will use these relations for the remainder of this work (see also the discussions in Koch et al. 2006).

In order to estimate the random and systematic measurement uncertainties on our derived coadded CaT metallicity, we performed a set of Monte Carlo simulations (e.g., Simon & Geha 2007), accounting for three effects. For this purpose, we added artificial Poisson noise to theoretical spectra, consisting of three Penny lines with line strengths representative of typical red giants as expected in our M31 sample. This noise addition accounts for the spectral quality in terms of the  $S/N$  ratio and the variance of the continuum. Secondly, we also added additional random noise peaks and troughs on top of the individual CaT lines, thus simulating potentially bad sky subtraction residuals that hamper CaT measurements. Even if one were to assume that the individual line profiles were perfect Penny functions, the (weighted) sum will not necessarily be a Penny anymore. By thus measuring the simulated coadded spectrum and comparing the obtained line strength with the traditional strength of the individual theoretical line profiles in the unperturbed spectrum according to eq. 3, we can finally estimate the influence of random noise, residual noise peaks and deviations from the assumed analytical line profile. In this vein, we adopt the standard deviation of the difference of the measured  $\langle\Sigma W\rangle$  in the noise added spectrum and the  $\Sigma W$  of the input spectrum as a measure of the measurement uncertainty as a function of the spectral  $S/N$  ratio and continuum variance. Thus Fig. 8 depicts the resulting relative uncertainty estimates. Typically, the widths measurements are accurate to the 15% level at a  $S/N$  of 10 and the relative error on the widths,  $\sigma\langle\Sigma W\rangle/\langle\Sigma W\rangle$ , generally does not exceed 25% at the spectral quality of our DEIMOS data. Applying our calibration from above (Eqs. 5,6), this translates into typical metallicity errors of (0.32,0.25,0.2) dex at  $S/N$  of (5,10,20). As another potential source of uncertainty, we estimate that a conservative continuum placement error of 2% will result in metallicity errors less than 0.1 dex.

Spectra with too low a  $S/N$  ratio to even measure the coadded line strengths were discarded from our sample on the spot so that we end up with a total number of 1673 CaT measurements (Table 2). An aggravating factor for using the CaT as a proxy for metallicity is the onset of strong TiO absorption in the coolest stars. Increasing strength of the TiO band at 8500Å progressively

depresses the CaT lines for redder stars so that the line strength  $\Sigma W$  starts to turn over towards lower values for colors redder than  $V - i' \gtrsim 2$  (e.g., Garnavich et al. 1994; their Fig. 13). This ambiguity, which also reflects in an overturn of the RGBs of metal rich globular clusters, prompted us to only include stars with  $V - i' \leq 2$  in the present chemical analysis. In this way we avoid an underestimate of the metallicities of the reddest stars. Thus 64 *giant stars* with velocities compatible with the M31 mean were removed from the CaT sample. We note that most of the reddest, nominally most metal poor stars that were thus rejected, are mostly found within  $\sim 40$  kpc so that they do not affect our later conclusions about the overall large-scale radial metallicity distributions.

### 5.1. On photometric metallicities

As a secondary estimate, we derived photometric metallicities of our stars by following isochrone fits laid out in Reitzel & Guhathakurta (2002). For this purpose we adopted individual corrections for reddening from the Schlegel et al. (1998) maps. In practice, we fit a set of isochrones to our CMD (Fig. 3), where we employed the stellar tracks without  $\alpha$ -enhancement from the Padova group (Marigo et al. 2008). Our choice to neglect  $\alpha$  enhancement is justified by the age range in M31's halo (Brown et al. 2006): Stellar populations with a wide age range have had sufficient time for supernovae of type I to contribute iron and therefore the composition trends toward Solar. Each star's locus in the CMD was then fit by a surface, using a 12th order function in both  $g' - i'$  and  $i'$ , with full cross terms, to the metallicity. In practice, we generated a grid of isochrones from the group's web-interface<sup>13</sup>, covering  $0.0001 \leq Z \leq 0.03$  with a spacing of 0.001. Moreover, we adopted the set corresponding to a population of 12.7 Gyr age, in concordance with the oldest populations found in the M31 halo (but see also Brown et al. 2003, 2006, 2007).

As the comparison with our CaT measurements in Fig. 9 indicates, the dwarf stars clearly deviate from unity, while the metallicities from both methods agree better for the giant candidates, albeit with a broad scatter (see also Kalirai et al. 2006a). The overall agreement within this scatter is notable down to the lowest metallicities. We will exclusively rely on our *spectroscopic* metallicities throughout this work, since the photometric metallicity estimates are generally prone to a number of inconsistencies: Among these are the strong influence of photometric uncertainties. The median error on our colors is 0.05 mag, but it reaches  $\sim 0.15$  mag for a number of our targets. For the more metal rich stars, the *formal* metallicity errors due to photometric errors are below 0.05 dex, but they exceed 0.1 dex for stars bluer than a  $g' - i'$  of  $\sim 1.5$  and can reach as high as 0.5–1 dex for the bluest giants. In this locus, the more metal poor isochrones become more and more degenerate and do not permit a reliable metallicity determination (see Fig. 3). In contrast, the CaT method has its greatest sensitivity at the metal poor end.

For populations with  $[\text{Fe}/\text{H}] > -1$  dex, the red giant branch curves both red and faint in a complex way, due to the onset of TiO absorption in the coolest stars (e.g.,

<sup>13</sup> [http://stev.oapd.inaf.it/\\\$sim\\$lgirardi/cgi-bin/cmd](http://stev.oapd.inaf.it/\$sim$lgirardi/cgi-bin/cmd)

Garnavich et al. 1994). This behavior is not well modeled and certainly affected by  $\alpha$ -enhancement. The assignment of metallicity becomes a complex function of both color and magnitude. Moreover, the systematic uncertainties on the photometric metallicities will be inevitably large, given the *a priori* unknown age- and abundance distribution of our stellar sample that is drawn from a patchwork of M31's populations. In this context, the presence of a broad distribution in stellar ages has been confirmed within the inner spheroid fields by the deep HST/ACS based CMDs of Brown et al. (2003, 2006, 2007), where in fact 30% of the stars in minor axis fields at 11 and 21 kpc were found to be 6–8 Gyr old.

Likewise, the unknown effects of varying distance modulus (Ibata et al. 2007) can easily move stars between different isochrones and pose an additional source of uncertainty. A plausible distance modulus spread of 0.5 mag translates into a 0.12 dex variation in the spectroscopic metallicities. This uncertainty in the stellar magnitudes will have, however, much larger effect on the photometric values. We will return to the issue of photometric metallicities in Sect. 7.1.

## 6. VELOCITY SUBSTRUCTURES

We shall now turn to the analysis of the dwarf cleaned M31 velocity distribution. For this purpose, we compare our observed data to a new suite of  $N$ -body simulations.

### 6.1. Simulating satellite accretion into M31's halo

In a new set of  $N$ -body simulations by Mori & Rich (2008) a satellite galaxy is accreted onto M31, for which the self-consistent potential of Widrow et al. (2003; their model A) was used. This potential is essentially a three component disk/bulge/halo model, the parameters of which were optimized to match M31's rotation curve and its surface brightness and velocity dispersion profiles.

Mori & Rich (2008) adopt the orbit of Fardal et al. (2006), which was originally constrained to reproduce the stellar distribution of the observed giant stream. For the accreted galaxy itself a total mass of  $10^9 M_\odot$  distributed as a Plummer sphere with a scale radius of 1 kpc was used. The progenitor mass can in general be well constrained by means of the observed thickness of the M31 disk (at  $z_d=300$  pc; Kuijken & Dubinski 1995) – excessive masses would have led to an early destruction of the thin disk component as we observe it today. In practice, the disk was represented by  $7.4 \times 10^6$  particles with a total mass of  $7 \times 10^{10} M_\odot$  and a scale length of 5.4 kpc. The bulge mass was assumed as  $2.5 \times 10^{10} M_\odot$  ( $2.6 \times 10^6$  particles), whilst the halo contained  $3.2 \times 10^{11} M_\odot$  ( $30.8 \times 10^6$  particles) with a tidal radius of 80 kpc. Yet, there is generally a significant lack of knowledge about the outer density profile of the dark matter halo. Therefore, one cannot avoid ambiguities in estimating the tidal radius and the total halo mass. In particular, the model of Mori & Rich (2008) has a smaller radius and mass compared to those of earlier studies (cf.  $8.8 \times 10^{11} M_\odot$  and a radius of 195 kpc; Fardal et al. 2007). However, since the satellite orbit is mainly followed within 50 kpc from the center of M31, the outer structure of the dark matter halo is of little relevance to the dynamics of the satellite.

In fact, the Mori & Rich (2008) simulation gives results similar to those of Fardal et al. (2007) who have a more

massive dark matter halo, but which otherwise have the same satellite orbit and position (by construction) and similar disk and bulge mass.

Apart from the vastly increased number of particles in the work of Mori & Rich (2008), the novelty of these simulations is the use of a self-gravitating, *live* disk and bulge that respond to the actual infall by particle motions of the underlying components. Thus we cannot only trace stars that were torn from the satellite in the course of the accretion, but also follow the fate of mutually removed disk and bulge stars. Hence we may assess how ejected disk stars might contribute to the halo in comparison to stars originating in the disrupted satellite. Another important feature of including the live disk and halo is that an accounting can be made of energy input into these populations from the collision event. This aspect affects the kinematics of the satellite's stars following the collision.

Projections of the simulation at  $t = 1$  Gyr in the standard M31 coordinate system are shown in Fig. 10, separately for disk, halo and satellite particles, as well as the combined simulation data. As these plots show, the main features observed in surface density maps of M31's halo, such as the Giant Stellar Stream (Ibata et al. 2001) and the bubble-like feature in extension of the stream (the Eastern and Western shelves; Ferguson et al. 2002, 2005; Irwin et al. 2005; Ibata et al. 2007) are well reproduced by the simulations.

### 6.2. Minor axis fields

The results from our simulations are shown in Fig. 11, in comparison with the observed distribution of stars on the minor axis in the analogous velocity vs. location space. It is evident that the simulations yield a characteristic triangular shape of the satellite particles' velocity as a function of projected distance, indicative of its disruption during the accretion (e.g., Merrifield & Kuijken 1998). This feature is also discernible in our observed data (top panel), though to a lesser extent, and is consistent with the findings of kinematically cold, i.e., low-radial velocity dispersion, localized substructure in Gilbert et al. (2007). While the simulations predict the maximum density of this shell-like feature to occur at a projected distance of  $\sim 1.4^\circ$  (19 kpc), the observations indicate an onset of this cold structure slightly inwards, at  $\sim 1.1^\circ$  (15–16 kpc). Using the Kayes Mixture Modeling algorithm of Ashman et al. (1994), we decomposed the (unbinned) velocity data at this location into two Gaussian components, thereby verifying the likely presence of a considerably colder substructure with a radial velocity dispersion of  $(29 \pm 22)$  km s $^{-1}$  plus an underlying canonical halo component with a dispersion of  $(110 \pm 10)$  km s $^{-1}$ . The population ratios, by number, of these components are 24% vs. 76%, in good agreement with Gilbert et al. (2007). It has been suggested by Gilbert et al. (2007) and Fardal et al. (2007) that such kinematic substructure is probably a realization of spatially localized shelves, which may provide the forward continuation of the giant stream. Other kinematic substructures other than the distinct V-shape in our data towards the inner spheroid are less conspicuous and the inner regions in our observations appear smoother compared to both the simulations and in the sample of Gilbert et al. (2007).



### 6.3. Outer halo fields

Although the radial scale in Figs. 11 and 12 (top panel) was chosen so as to emphasize the substructure and build-up of the inner halo within  $\sim 35$  kpc, we note that we detect stars that were flagged as genuine M31 red giants out to large radial distances of 160 kpc (see Fig. 12, bottom panel), thus strengthening the claim for the large radial extent of M31's stellar halo by Guhathakurta et al. (2006) and Kalirai et al. (2006a). Nevertheless, the number density of confirmed members at large radii is sparse (these are addressed in further detail in Fig. 19). The outermost field at 160 kpc (m11) contains 16 giant candidates with a mean velocity of  $-180 \text{ km s}^{-1}$ , nine of which lie above  $-200 \text{ km s}^{-1}$  and seven with velocities in excess of  $-150 \text{ km s}^{-1}$ . In the adjacent, second most remote field (m8), seven stars survived the criteria for being selected as giants, although only one exhibits a radial velocity close to M31's systemic mean, while the remainder shows velocities between  $-180$  and  $-120 \text{ km s}^{-1}$ , thus about of the order of  $1.2\text{--}1.8\sigma$  above M31's mean velocity. While we cannot exclude the possibility that these stars are in fact members of M31's outermost, extended halo, we labeled their mean velocities as upper limits in Fig. 12 (bottom). All in all, there is a progressively larger relative contribution of stars at higher velocities with respect to M31's mean towards outer fields. Based on their star count maps, Ibata et al. (2007) estimate that the field covered by our four m11 masks should contain 0–2 M31 red giants. In fact Kalirai et al. (2006a) report on the presence of 3 bona fide giants in this field. Given the location of this field at a separation of  $4^\circ$  ( $\sim 50$  kpc) of M33, it is then conceivable that the stars towards the higher velocity tail are part of the overlapping, extended halo component of M33, as suggested by Ibata et al. (2007). With its distance from the Sun of 849 kpc (Galleti et al. 2004), M33 is located at a distance of 220 kpc from M31 (e.g., Koch & Grebel 2006) and its systemic velocity lies at  $-180 \text{ km s}^{-1}$  (e.g., McConnachie et al. 2006). Judging by the surface brightness profiles of Ibata et al. (2007; e.g. their Fig. 28), the contribution of M33 stars (coupled with the inevitable foreground component) appears to set in at radial distances  $\gtrsim 11^\circ$  ( $\sim 150$  kpc).

### 6.4. The halo's merger origin

It is then intriguing to ask, to what extent the full halo of M31 has been assembled via the accretion of one or more accretion events such as the one simulated in Mori & Rich (2008). Is there a necessity to invoke more such mergers or is there evidence of several disruptive events involving many smaller satellite systems? In fact, Ibata et al. (2007) have revealed a wealth of substructures and stellar streams that haunt the full extent of M31's halo, thereby complicating the interpretation of this halo as a single, smooth entity. Therefore, we show in Fig. 13 our observed radial velocity distributions against the simulated ones as a function of radial distance. The simulation particles shown were selected from locations that coincide with our observed fields, but we inflated the respective selection boxes, where necessary, so as to ensure the same number of observed and simulated stars for the comparison.

The first thing to note is the presence of two major

velocity peaks in the simulated data, which reflects the wrap of the material stripped from the disrupted satellite galaxy around the M31 disk, as is in fact observed in the form of the Giant Stellar Stream. The regions of the aforementioned cold substructure are contained within the  $R = 17$  kpc histogram, yet there is no clear resemblance between observations and simulations in this regard. While the simulations still show the apparent kinematic bifurcation with pronounced peaks at  $-400$  and  $-200 \text{ km s}^{-1}$ , the observations indicate the narrow population peaking at M31's systemic velocity of  $-300 \text{ km s}^{-1}$ , with an underlying, smoother and broader genuine halo population. To this end, we also plot in Fig. 13 (dashed lines) the contribution of original M31 halo stars from our simulation (again selected from the same spatial locations as above), i.e., those, which are not related to the disrupting satellite in any way. It is striking that a major part of our velocity histograms at all radii closely resembles this genuine halo component, and that the strongest deviations of the velocity distributions from the simulations occur towards the fields at approximately 13–17 kpc. Furthermore, there is a clear discrepancy between the model predictions and the observed distribution in the innermost spheroid ( $\lesssim 13$  kpc). This kinematic evidence suggests that the inner spheroid of M31 cannot entirely consist of debris from one collision like the one responsible for the Giant Stellar Stream. In fact most of the observations at all radii appear to strongly overlap with the prevalent M31 halo component, again showing that the accretion of a massive satellite galaxy did presumably not single-handedly drive the build-up of the inner halo of M31.

Moreover, the discovery of at least 4 major streams perpendicular to M31's minor axis, which also intersect our observed fields (Ibata et al. 2007) clearly shows that essentially all of our targeted fields are contaminated by a more or less significant fraction of stars originating in the mergers of the systems responsible for these streams (Chapman et al. 2008). Although the exact shape of the simulations' velocity distribution depends on the extensive parameter space of progenitor structure, its kinematics and orbit, the overall trends and discrepancies between model and observations discussed above will not sensitively rely on such parameter variations and are expected to persist, in particular, since the Mori & Rich (2008) model reproduces the structural features in the halo observed in the surface brightness maps remarkably well.

The observed velocity distributions (Figs. 12,13) in the Giant Stream fields H13s and a3 (at 21 and 32 kpc) show the clear signatures at  $-520$  and  $-400 \text{ km s}^{-1}$  (H13s) and  $-450 \text{ km s}^{-1}$  (a3). In accordance with Kalirai et al. (2006b) we find the H13s peak at  $-520 \text{ km s}^{-1}$  to be more prominent relative to the one at higher velocities. It is then noteworthy that, while well predicting the Stream component at  $-400 \text{ km s}^{-1}$  at  $\sim 17$  kpc (bottom left panel of Fig. 13), our simulations and the models of Fardal et al. (2006, 2007), on which our orbit is based, fail to reproduce the primary, low-velocity peak prominently seen in the 22 kpc histogram, as well as the outer stream field in the data 30 kpc. This feature is, however, well reproduced by the simple orbit model by Ibata et al. (2004).

Interestingly, neither disk, nor bulge stars, ejected during the simulated merger event contribute any considerable fraction to any of the potential substructures in the velocity histograms. Only a few of these ejected disk stars are to be found within the innermost 10 kpc: The number ratios of model particles within a region corresponding to the observed field f109 are 0:2:280:1 (bulge/disk/halo/satellite). None of the disk particles ventures any further out. At a total of 158 giant stars in this field, we would expect no more than 1–2 stars ejected from the M31 disk.

## 7. ABUNDANCE SUBSTRUCTURES – A STRONG GRADIENT

In Fig. 14 we show our metallicity results from the new coaddition measurements (Sect. 5) as a function of radial velocity and radial distance. It is worth noticing that the distribution of these spectroscopic metallicities with velocity (left panels) appears to be a powerful dwarf/giant discriminator that can be efficiently employed in cases, where not all of the traditional indicators are available (cf. Sect. 4). In this representation, the dwarf stars occupy a narrow range above  $\gtrsim -150 \text{ km s}^{-1}$  around “[Fe/H]”  $\sim -2$  dex. Given the lack of knowledge of their distances, their assignment relative to a HB magnitude becomes meaningless. It is also far from self-evident that the CaT linestrength correlates with metallicity in the dwarf stars as in the giants. For this reason, the traditional calibrations (Rutledge et al. 1997a, 1997b; eqs. 5,6) are not valid for dwarfs anymore and their application leads to their clear separation in Fig. 14.

Contrary to the strong clumping in velocity space (Figs. 11,12), there is no apparent population substructure discernible within the inner fields of  $R \lesssim 20$  kpc, nor in the Stream fields at 21 and 32 kpc. More striking is the sudden decrease in the mean metallicity towards larger projected radii that becomes already visible in this representation. It is at these distances, where a transition from the dominant, more metal rich bulge population towards a more metal poor halo component may occur (Ostheimer 2003; Kalirai et al. 2006a). This view would also conform with the claim of a break in M31’s surface brightness profile between an inner  $R^{1/4}$  profile (de Vaucouleurs 1958) and a gradual transition to an  $R^{-2}$  power-law surface brightness profile that defines an outer halo (Irwin et al. 2005; Guhathakurta et al. 2006; Chapman et al. 2006). Interestingly, the run of the strength of the TiO band<sup>14</sup> at  $7100 \text{ \AA}$  (top left panel of Fig. 15) lends strong support to this scenario. While a number of TiO-strong, thus more metal rich, giants are predominant in the bulge and inner halo regions, these are clearly missing in the outer parts beyond  $\sim 50$  kpc.

In Fig. 15 (top right panel) we separate our full data set into three radial bins, comprising the inner spheroid ( $R < 20$  kpc), the transitional region (20–40 kpc) and the outer halo fields from 40 kpc out to our last data at 160 kpc. There is a clear indication that the outer fields are distinctly more metal poor by more than 1 dex compared

to the inner spheroid: while the inner 20 kpc’s metallicity distribution function (MDF) peaks at  $\sim -0.6$  dex, the mean metallicity shifts progressively towards  $\sim -1.2$  dex for  $20 \text{ kpc} < R < 40 \text{ kpc}$ . This region already contains a considerable component below  $-2$  dex, which becomes the characteristic metallicity regime in the outermost fields. A K-S test reveals that the MDFs from all three regions are unlikely to originate from the same parent distribution, with all probabilities being consistent with zero. This suggests that there is in fact a mixture of populations, possibly from the inner spheroid and an outer halo component. Nevertheless, we note that the dispersion of the MDF (as derived from an iterative Gaussian likelihood estimator accounting for measurement errors; Koch et al. 2007) does not increase considerably due to the potential overlap of two populations of separate peak metallicities: at  $(0.47 \pm 0.02)$  and  $(0.46 \pm 0.03)$  the dispersions are practically indistinguishable. However, it is perilous to compare these numbers, when splitting the sample in only these two regions along a broad spatial range.

Thus we plot in the middle panel of Fig. 16 the dispersion in metallicities versus radius in smaller radial bins that were, for  $R < 40$  kpc, chosen such as to maintain the same number of stars (viz. 100). This way, we guarantee a proper statistical sampling; furthermore, since the data were analyzed in a homogeneous manner, no systematic biases will be introduced when averaging data across adjacent masks. Only for the three outermost fields beyond 85 kpc do we group the sparse data by field (11, 5, and 10 giants in m6, m8, and m11) to avoid averaging across the large radial gap. These fields are separated by 40 kpc (already the size of the entire inner spheroid) and it is further likely that these fields are contaminated by both substructure and the halo of M33.

The bin at 16 kpc shows a metallicity dispersion that is higher by 0.24 dex than the average, while the adjacent bin at  $\sim 18$  kpc again exhibits an average dispersion. It is worth noticing that the dispersion in our data around 13–14 kpc shows a remarkably smaller internal (i.e., accounting for measurement errors) dispersion in  $[\text{Fe}/\text{H}]_{\text{CaT}}$  of  $\sigma = 0.21 \pm 0.03$  dex (at a mean metallicity of  $-0.84 \pm 0.07$  dex). In fact, this region corresponds to the approximate location of the kinematic substructure discussed in the previous section and by Gilbert et al. (2007). Without applying any further velocity cuts to extract substructure stars by isolating their triangular distribution in velocity space, these regions are expected to contain an overlap of giants from the intrinsic inner spheroid population and those forming the substructure itself. As Gilbert et al. (2007) argue, the resulting, intermixed MDF should be expected to be slightly more metal rich than adjacent other fields. The radial bin in question is slightly more metal rich on average by  $\sim 0.11$  dex than the next inner data (at a significance of  $0.9\sigma$ ). Hence, our mean abundances in the inner spheroid and the substructure do not lend strong support to the cold structure being significantly more metal rich than its surroundings.

However, the mean  $[\text{Fe}/\text{H}]_{\text{CaT}}$  significantly drops by about 0.4 dex ( $2.5\sigma$ ) between approximately 16 and 20 kpc (Fig. 16), while this trend even proceeds further outwards. We note that this sharp drop coincides with the edge of disturbed region visible in the Ferguson et al.

<sup>14</sup> The TiO<sub>7100</sub> band pass is a classical discriminator of spectral types (O’Connell 1973) and we measure its strength by a straight integration of the line band pass from 7055–7245 Å with respective continuum bands. Larger values of TiO<sub>7100</sub> indicate the presence of cool, metal rich giants.

(2002) maps. As Ibata et al. (2005) show, the majority of the photometric contrast in the Ferguson et al. (2002) maps, leaving the impression of an edge, is due to an extended, rotating disk component (see also Fig. 1, top panel). As this structure has a high  $[\text{Fe}/\text{H}]$ , the transition that we map in the metallicities is mostly a result of moving off the rotating component and into the underlying halo dominance, where the halo falls off much more slowly than the exponential disk.

Beyond 40 kpc, the MDF contains 108 stars (Fig. 15, top right), but it is evident that the majority of these M31 red giant candidates are more metal poor than the crossover region by  $\sim -1$  dex. In particular, the 60 kpc fields provide a transition from the metal poor outermost fields and the more metal rich inner parts, which is to be expected as they are dominated by the more metal rich tangential streams they lie on (see Fig. 1, bottom panel; Chapman et al. 2008). All in all, there is a pronounced metallicity gradient seen throughout our fields within M31's spheroid, which becomes even more striking in the plot of individual metallicities as a function of distance from M31 (bottom panel of Fig. 15).

### 7.1. Comparison with previous detection of a gradient

A distinct metallicity gradient in M31's halo has already been proposed by Kalirai et al. (2006a), who find a more gradual leveling of their MDFs, based on *photometric* metallicities, from  $-0.47$  dex within 20 kpc to  $-0.94$  dex around 30 kpc down to  $-1.26$  dex beyond 60 kpc (open squares in the top and bottom panels of Fig. 16). Thence their data imply a smooth decline as  $(-0.77 \pm 0.09)$  dex  $(100 \text{ kpc})^{-1}$ . The analysis of our data, on the other hand, yields a steeper radial metallicity gradient of the order of  $(-1.50 \pm 0.08)$  dex  $(100 \text{ kpc})^{-1}$ . Our finding of a clear abundance gradient is underscored by the disappearance of TiO strong, metal rich giants in the outermost fields (Fig. 15, top left panel). In fact, the outermost radii appear to be dominated by a purely metal poor population. Another significant difference between the gradients derived in this work and suggested by Kalirai et al. (2006a) is the overall lower metallicity at almost any given radius in our analysis. On average, our *mean* abundances in those fields in common with their data are more metal poor by 0.75 dex. Given the quoted measurement errors from both sources, this discrepancy is significant at the  $3.4\sigma$  level and the reason for such a deviation merits careful investigation.

In the top panel of Fig. 16, we only include the minor axis data, which were radially binned such as to guarantee the same, statistically significant number ( $\sim 100$ ) of stars per bin. Our data and those of Kalirai et al. (2006a) additionally includes off-axis fields, which we highlight with the encircled points in the top panel of Fig. 16. Two of these are located directly on the Giant stream (H13s and a3), while also a13 and b15 fall towards the edge of the stream feature at a projected distance of  $\sim 50$  kpc. It is known from previous spectroscopic measurements (Guhathakurta et al. 2006; Kalirai et al. 2006b) that the stream is intrinsically more metal rich than the halo. One other field in Kalirai et al. (2006a) lies on the dwarf spheroidal (dSph) galaxy And III (d3), which exhibits a population representative of M31's moderately metal poor satellite galaxies (with a mean abundance of  $\sim -1.7$  dex; McConnachie et al.

2005). As the field may well be contaminated with dSph members, we do not consider it a representative choice for a study of the pure M31 halo. Due to our inclusion of the inner spheroid fields, we have significantly greater numbers within 20 kpc. In order to evaluate the influence of the off-axis fields on the metallicity gradient, we include in the bottom panel of Fig. 16 all our measurements throughout M31's spheroid, separated by field (see also the color coded map in Fig. 1, bottom panel). These fields include H13s, a3, a13, a19 and b15, which were also targeted by Kalirai et al. (2006a). Nevertheless, it is obvious that the strong character of the gradient persists disregarding whether we focus on the minor axis or on the whole spheroid. Thus the metallicity gradient is likely a characteristics associated with M31's full halo.

One major source of uncertainty is in general the use of photometric metallicities. Larger photometric errors, the choice of the adopted set of isochrones, the general failure of stellar evolutionary tracks to simultaneously reproduce the major features of CMDs (Gallart et al. 2005; and references therein) and undesired age-metallicity degeneracies on the RGB render photometry the less reliable metallicity indicator as compared to spectroscopic estimates. Isochrone fits produce values for the actual stellar metallicity,  $Z$ , which incorporates the admixture of heavy elements, in particular the  $\alpha$ -elements. In this vein, any unknown  $\alpha$ -enhancement can considerably alter the derived photometric metallicities. Kalirai et al. (2006a) demonstrate that an  $[\alpha/\text{Fe}]$  ratio of  $+0.3$ , as found in the Milky Way halo, yields results more metal poor by 0.22 dex compared to those derived from scaled-solar isochrones (but see also Koch et al. 2006 for a discussion of the systematics of  $\alpha$ -variations on CaT metallicities). In order to reconcile the spectroscopic (this work) and photometric (Kalirai et al. 2006a) metallicities a strong enhancement in these elements of at least 1 dex would be required. This seems an unreasonably high value, even if the formation of the outer halo regions were dominated by early star formation bursts.

Photometric metallicities are especially susceptible to overestimating the metallicities of metal poor stars. For stars with  $[\text{Fe}/\text{H}] < -1.5$  dex, there is relatively little difference in the metal line blanketing in the V band: In color-magnitude diagrams such as Fig. 3, a 1 dex decrease in metallicity causes little discernable change in color. Given that for many distant systems, the only accessible metallicity estimate is photometric metallicity, we would thus urge the use of bluer filters, and greater caution in the interpretation of results. It is reassuring, though, that despite the large overall discrepancy between the Kalirai et al. (2006a) and our measurements, there is a significant agreement between the two studies in field m8 (at 120 kpc). In this field, we find 7 giant candidates, for 5 of which we could measure an  $[\text{Fe}/\text{H}]_{\text{CaT}}$ . If we discarded those two stars with the largest velocities that are in the transition higher-velocity tail of our distribution ( $\sim 1.2$ – $1.5\sigma$  above the systemic mean), the mean abundance would even drop by another 0.1 dex, confirming the dominance of metal poor of stars in these outer fields. We note in passing that m8 constitutes one of the fields for which Ibata et al. (2007) exclude the occurrence of any substructure, so that it may in fact be a contender for representing M31's genuine underlying metal poor halo (see also Chapman et al. 2006, 2008).

Finally, we add to Fig. 16 the mean spectroscopic  $[\text{Fe}/\text{H}]$  in a minor axis field at 19 kpc, based on the 29 confirmed red giant members of Reitzel & Guhathakurta (2002; their Fig. 17). These authors not only find that their spectroscopic metallicities are systematically lower than the photometric counterparts, but they also detect a distinct metal poor tail in this MDF, reaching as low as  $[\text{Fe}/\text{H}]_{\text{CaT}} = -2.85$  on the scale of Carretta & Gratton (1997). By comparing their MDF to those of Galactic and M31 globular clusters and of Local Group dSph galaxies, they attributed its shape and the presence of such metal poor stars to the build-up of M31's halo from the accretion of many a small subsystems. As this comparison with our data shows, the mean metallicity in the Reitzel & Guhathakurta (2002) field is in good agreement with our measurement in the respective radial bin. The most recently discovered faint dSph satellites around M31 are predominantly characterized by mean metallicities between  $-1.3$  and  $-1.7$  dex (Martin et al. 2006b; Majewski et al. 2007), which agrees well with the field star population's abundance over a radial range from  $\sim 20$ – $50$  kpc.

### 7.2. Andromeda's metal poor outer halo

In contrast, the significant discrepancy of the mean metallicity estimates in the outermost field, m11, is an issue of concern: While Kalirai et al. (2006a) state a value of  $\sim -0.92$  dex from their three confirmed red giant members, we find a value as low as  $\sim -2.6$  dex from 10 red giant candidate stars in total. It is then fair to ask *how reliable are our low metallicities* in this highly foreground contaminated field and how trustworthy is our detection of metal poor stars at all radii? First, if those marginal stars with potentially too high velocities were removed from m11, the mean value in this field would essentially remain unaltered – *the metal poor nature and strong gradient do persist*. All in all, there are 56 stars with  $[\text{Fe}/\text{H}]_{\text{CaT}} < -2.3$  found at all radii from 9 to 160 kpc. Based on their higher radial velocities, no more than 6–8 of these could be potential remaining foreground contaminants. Furthermore, it was verified by visual inspection that none of the stars is a potential mismatch in spectral type or exhibits spurious noise peaks. Also, we note that the median log-likelihood  $L$  (Sect. 4) amounts to 0.7 for these stars so that it is 5 times more likely that they are M31 red giants than Milky Way stars based on the adopted discriminant indicators. As we have shown in Sect. 4.1, there may be  $\sim 35$  undetectable blue dwarfs in our whole sample (Table 2), based on the Besançon predictions. Furthermore, the model predicts that only 15% of these stars have nominal metallicities below  $-2.3$  dex, which translates into  $\sim 5$  such undetectable contaminants in our sample.

The principal caveat against deriving a metal poor tail in stellar populations is that, generally, no calibrations of the CaT strength exist below  $-2.1$  dex. Neither the original sample of Rutledge et al. (1997a, 1997b) included any system more metal poor than  $-2.02$  dex (on the scale of Carretta & Gratton 1997), nor did our calibration clusters (Fig. 7). Nevertheless, the CaT technique is widely applied throughout the literature of metal poor stellar populations and can still maintain its prime role in at least a relative ranking of stars towards the metal poor extrapolations (Koch et al. 2006; Simon & Geha 2007;

Battaglia et al. 2008)<sup>15</sup>. We plot in Fig. 17 a series of spectra that were grouped and coadded in various metallicity bins. It becomes obvious that the expected trend of increasing CaT line strength with increasing  $[\text{Fe}/\text{H}]$  is also visible in our data so that our metallicity scale and ranking derived from the CaT coaddition did not introduce any grossly falsified results, in particular towards the metal poor spectra. This coaddition of the spectra also emphasizes a number of Fe I and Ti I lines that clearly scale with metallicity in our spectra and will allow us to estimate chemical abundance ratios in future works (see also Kirby et al. 2008).

As a further comparison, we generated synthetic spectra of red giants, using Kurucz model atmospheres<sup>16</sup> with representative stellar parameters, i.e., ( $T_{\text{eff}}=4000$  K,  $\log g=1.0$ ,  $\xi=1.5$  km s<sup>-1</sup>), and solar-scaled opacity distributions<sup>17</sup> (e.g., Koch et al. 2008). In Fig. 18, we show the resulting syntheses for different metallicities of the atmospheres. These spectra have been degraded to match the spectral resolution of DEIMOS and, in the bottom panel, convolved with an additional noise component to mimic a representative spectrum with  $S/N=10$ . Apart from the expected weakening of the CaT, there is a visible decrease in the strength of the weak Fe I absorption features (e.g., at  $\lambda\lambda 8514.1, 8468.4, 8621.6, 8674.7\text{\AA}$ ) adjacent to the CaT (see also Bosler et al. 2007) towards lower metallicities. This decrease is even discernible in the low  $S/N$  spectra and in fact observable in our coadded spectra (Fig. 17).

One might then argue that the metal poor stars could be an artifact of the new coaddition technique and its calibration devised in Sect. 5. To test this, we grouped the spectra of progressively metal poor stars, and applied the same method as before on the coadded spectra. It transpires that the metal poor character of these spectra persist and there is a tight, close-to-unity relation between the metallicity bin of the individual stars to be grouped, and the final coadded estimate from the coadded spectra. Moreover, the use of our own consistent calibrations (eqs. 5,6) does not alter the qualitative detection of metal poor stars: if we were instead to use the canonical calibration of Rutledge et al. (1997a, 1997b), we would observe a shift of the measurements towards  $[\text{Fe}/\text{H}]$  lower by 0.2 dex at  $-3$  – if anything, our calibration would overestimate the metallicities so that the metal poor character of the distribution remains. Further tests that we employed to ascertain the reality of the gradient and the metal poor stars verified that there is no unusual trend of the  $[\text{Fe}/\text{H}]$  with magnitude discernible, nor does the gradient change when we restrict the analyses only to the high- or low- $S/N$  spectra, respectively. Moreover, to test the influence of potential remaining dwarf contamination, we constructed another test sample by only including stars with radial velocities below  $-300$  km s<sup>-1</sup>. Apart from increased statistical uncertainties due to the decreased sample size, the outer

<sup>15</sup> The same holds for the calibration of metal rich stars: the most metal rich globular cluster in our sample, M5, has  $[\text{Fe}/\text{H}]_{\text{CG97}} = -1.12$  dex), while a small fraction of our measured M31 stars nominally reach above solar values. That the CaT calibration is still valid up to  $+0.47$  dex has recently been demonstrated by Carrera et al. (2007).

<sup>16</sup> <http://kurucz.harvard.edu>

<sup>17</sup> <http://wwwuser.oat.ts.astro.it/castelli>

regions do remain metal deficient and the gradient perseveres. On average, the “pure”, velocity restricted giant sample yields mean metallicities in each field that are more metal poor by 0.04 dex (r.m.s. scatter of 0.50 dex) on average than the full giant data. Essentially, the same holds if we inflict a strict color cut to select a “pure” giant sample: a gradient persists even for a, say,  $V - i' > 1$  subset. Neither are any significant changes found if we restrict the analysis only to giants classified as such in  $> 95\%$  of the Monte Carlo runs of the dwarf/giant separation (Sect. 4). The median difference between the mean metallicities from “all” giants and the  $2\sigma$  cases is  $< 0.01$  dex (r.m.s. 0.08 dex). Moreover, our dwarf sample does not exhibit any significant sign of a gradient (at  $0.06 \pm 0.04$  dex  $(100 \text{ kpc})^{-1}$ ), which is expected, since the CaT is no metallicity indicator for these stars so that their  $[\text{Fe}/\text{H}]$  are randomly distributed.

The color coded CMD in Fig. 3 then verifies that the trend of metallicity with location on the RGB is in fact as expected, with the more metal rich stars (red points) exhibiting progressively redder colors, and the most metal poor stars (blue points) being predominantly located towards blue colors. We also note the presence of  $\sim 40$  giants that fall bluewards of the most metal poor isochrone in Fig. 3. Given our discussion in Sect. 4.1, it appears unlikely that these are Galactic contaminants. Although their spectroscopic metallicities indicate them to be metal poor objects, their remarkably blue colors are surprising. If one were to assign these colors to erroneous photometry, and thus redden these objects towards the  $[\text{Fe}/\text{H}] = -2.3$  isochrone, this color difference translates (Eqs. 5,6) into a spectroscopic metallicity uncertainty of less than 0.30 dex with a median of 0.03 dex (r.m.s. scatter 0.09 dex). All in all, we are left to believe that there is in fact a detectable, real population of considerably metal poor red giants present in M31’s inner halo that becomes yet more prominent in its outer halo.

This fact then confirms the view of an accretion origin of the inner halo, presumably by several events, and argues strongly in favor of the same mechanism governing the formation of the inner and the outer halo. Moreover, there is additional evidence (Chapman et al. 2008, in prep.) that halo fields at 110 kpc are not affected by any of the substructures in the Ibata et al. (2007) maps and are consequently a plausible true halo component; they are found to have  $[\text{Fe}/\text{H}] \sim -2$ .

Given that the halo of M33 itself is also metal poor (at around  $-1.5$  dex; McConnachie et al. 2006) it is again feasible that a major fraction of the red giants in the outermost fields, are members of M33, the more so, since their velocities appear to be similar to the systemic velocity of M33. At present, there is no compelling evidence against the hypothesis that *all* the candidate giants in these distant fields  $\gtrsim 120$  kpc are genuine M33 members. Fig. 19 (left panel) shows the metallicities and velocities of stars in the three most distant fields, where we schematically overplot each galaxy’s velocity distribution, using the stellar halo parameters from McConnachie et al. (2006) for M33 and those derived in this work for M31. Under the simplifying assumption that these fields contain an equal mix of M33 and M31 stars, we can estimate, based on our targets’ velocities, that 85% of the red giant members in field m11 and m8, and 37% of those

in m6, might actually belong to M33’s halo. Statistical removal of this contribution would yield mean metallicities of  $(-1.94 \pm 0.52, -2.00 \pm 0.60, -1.60 \pm 0.38)$  dex in m6, m8, and m11. However, there is no way of reliably separating the mutual overflow of giants into each other galaxy’s halo at present.

The more metal rich stars at  $[\text{Fe}/\text{H}] \gtrsim -1.2$  dex and velocities around  $-325 \text{ km s}^{-1}$ , on the other hand, might plausibly be considered to have originated in a radial collision, presumably like the one that bore the ancient Giant Stream (see Mori & Rich 2008). This hypothesis is also consistent with them being close to the systemic velocity of M31. In particular, there are no stars found with very high negative velocities relative to M31 – all giants in these fields have velocities well within  $\sim 1.5\sigma$  of the M31 mean in the negative velocity tail (which does account for M31’s radially decreasing velocity dispersion).

## 8. CONCLUSIONS

From a spectroscopic analysis of 1316 confirmed red giant stars along the minor axis on M31 and in spheroidal fields out to 160 kpc we find and confirm the following structural specific features in M31’s inner and outer halo:

1. There is evidence of an abundance substructure in the sense that the mean stellar metallicity strongly declines at  $\sim 20$  kpc, where the abundance range within this radius is typically  $-0.5$  to  $-1$  dex and falls towards  $-1.4$  dex at 20–40 kpc. The latter values are consistent with those detected within a smooth underlying M31 halo (Ostheimer 2003; Guhathakurta et al. 2006; Kalirai et al. 2006a; Chapman et al. 2006). Interestingly, the location of the break in the metallicity profile coincides with the edge of the metal rich, extended rotating disk reported by Ibata et al. (2005), but it cannot be entirely ruled out that there is also a contribution from the kinematic substructure (Gilbert et al. 2007), which would bias the inner regions towards marginally higher metallicities. A metallicity gradient has been detected by Kalirai et al. (2006a), but here we show that the decline in our spectroscopic measurements appears to proceed even stronger towards the outermost fields at 160 kpc, where we find mean values around and even below  $-2$  dex.
2. In particular, there is a considerable fraction of metal poor stars below  $[\text{Fe}/\text{H}]_{\text{CaT}} \lesssim -2$  found at almost all radii. Their presence is not utterly surprising, and red giants that metal poor have been claimed to exist in M31’s halo before (e.g., Reitzel & Guhathakurta 2002). Furthermore, their established prominence in the Milky Way halo (Carney et al. 1996; Chiba & Beers 2000; Carollo et al. 2007) raises the question, why there should not be a comparable distribution present in the M31 halo, if both systems had experienced a similar formation and accretion history.
3. A considerable fraction of stars in the outermost fields beyond  $\sim 100$  kpc (which corresponds to about 100 kpc projected distance to M33) exhibit velocities and metallicities consistent with those of M33 halo stars. This confirms earlier findings from

star count maps (Ibata et al. 2007), according to which the stellar halos of these major Local Group spirals overlap to a large extent.

4. We confirm the earlier detection of a kinematically cold substructure (Gilbert et al. 2007), located at a radial distance of 15–20 kpc. By comparison of new N-body simulations (Mori & Rich 2008), we show that such a substructure is consistent with having originated in the merger event that produced M31’s Giant Stellar Stream (Ibata et al. 2001, 2004). Nevertheless, the full radial velocity distribution along the minor axis is difficult to reconcile with a single collisional event of this kind, and it is more likely that a wealth of accretions occurred and formed the halo, which is concordant with the progressive detections of stream-like substructures in star count maps (Ibata et al. 2007).
5. There is a considerable contribution of stars from a genuine, ancient M31 halo, potentially ejected during such merger events, to the velocity distribution at any radius. Moreover, neither stars from the pristine bulge or disk components are likely to be found in the outer or even inner spheroids.

This leaves us with a picture in which the progenitor that produced the giant Stream and thus presumably donated a major part of M31’s halo cannot be single-handedly responsible for all the substructures seen in our and previous studies – outside the present-day Stream’s sphere of influence, one sees a predominant occurrence of minor substructures or streams from many a past mergers. A large number of accretion events is also thought to have contributed to the formation of M31’s disk (e.g., Peñarrubia et al. 2006), as this would produce the proper, observed mix of metallicities. Ibata et al. (2007) note that the radial metallicity gradient is a mere reflection of Stream debris and numerous other substructures in the *inner* regions, which is in concordance with model predictions. In this context the metal rich, genuine Stream material is more centrally concentrated, leaving the impression of a more extended underlying metal poor halo (cf. the stream distribution in Fig. 13). It is unclear at present, whether the gradient is intrinsic to the inner substructures becoming more metal poor with radius, or whether the underlying halo, with its larger dominance in the outer regions, is becoming more metal poor. Note that Brown et al. (2007) find that an HST field at 25 kpc ( $\sim 1.5^\circ$ ) is both more metal poor and older than the innermost HST field projected at 11 kpc. Hence, also the HST pointings appear not to be dominated by the canonical Stream’s debris. Moreover, we find that the innermost deep HST field (Brown et al. 2003) is situated in a region that has some potential contribution from tidal debris, but appears to be dominated by a more metal rich “inner halo” population with a *smooth* velocity distribution, free of the structures at the velocity extremes that are predicted to be present from interaction models (see left middle panel of Fig. 13). The Brown et al. (2003) 11 kpc field appears to be free of major contamination from an infall event. The 21 kpc field lies just outside of the metal rich inner region; Brown et al. (2007) suggest a lower metallicity for this field, which we confirm from our CaT analysis. The field at 35 kpc appears to be yet

more metal poor and may be genuinely representative of the outer halo. We note that all the HST fields at 11, 21 and 35 kpc have very different circular orbital periods (derived from a simple mass model and the assumption of circular orbits) of  $\sim 0.2$ , 0.5 and 1 Gyr, respectively. The characteristics of the HST deep fields will be discussed in a forthcoming paper (Rich et al. in prep).

Using the same arguments, we find large orbital periods of  $\sim 6$  Gyr at 160 kpc, which presupposes them to be bound to M31 (see also Majewski et al. 2007). It is hard to reconcile these time scales with a scenario, in which these distant M31 members are pressure supported. It is rather an attractive notion that these distant stars might be ejecta of collisions, not yet having completed a single orbit around M31.

The fact that the new metallicity scale we framed in this work is in good agreement with the moderately metal poor character of the dSph satellites of M31 (Reitzel & Guhathakurta 2002; McConnachie et al. 2005; Martin et al. 2006b; Majewski et al. 2007) further support the idea that the outer halo might plausibly emanate from a population similar to the dSphs. Moreover, the presence of the more metal rich stars beyond 100 kpc suggest an origin of these stars in collisions rather than in a primordial halo. Yet it is challenging to reconcile this scenario with the number count maps of Ibata et al. (2007), which are smooth to within the sensitivity of the MegaCam survey in these regions and with the presence of very metal poor stars: there are no very metal poor stars detected in the Galactic dSphs (Koch et al. 2006; Helmi et al. 2006), nor in the faintest M31 satellites (Martin et al. 2006b, 2007), so that it remains unclear whether systems like the present-day observed dwarf satellites are responsible for the bulk of the halo.

While our observed radial metallicity gradient stretches 1.5–2 dex over the full extent of our data of 160 kpc, simulations of the hierarchical assembly of Galactic halos do not reproduce any considerable gradients. In this context, the study of Font et al. (2006) predicts gradients in  $[\text{Fe}/\text{H}]$  averaged over each full simulated halo of at most 0.5 dex over a few tens of kpc.

Our findings lend striking support to paralleling the M31 and Galactic halos: In a recent work Carollo et al. (2007) detected a dichotomy in the Milky Way’s stellar halo. In this sense, there exists a clear kinematic and chemical separation into an inner halo (with stars on more eccentric orbits, metallicities around  $-1.6$  dex, a flattened density distribution and no considerable rotation) and an outer, independent halo component, which is more spherical in shape, shows evidence of rotation *and is more metal poor* on average. In particular, the outer Galactic halo exhibits a peak metallicity of  $-2.2$  dex. The presence of two distinct halos is well explicable in the context of cosmological structure formation models and incorporates the continuous, chaotic accretion of distinct subhalos that follow an earlier stage of the dissipative merging of massive, yet sub-galactic fragments (see Carollo et al. 2007 for a discussion of the detailed formation scenario). If structure formation proceeded in analogy to form M31 – and in the light of  $\Lambda$ CDM this is likely – then the clear distinctness of at least two halo components visible in the MDFs in our M31 study is a natural outcome of the accompanying stochastic abundance accretion.

As a concluding, independent remark, we note that a further benefit of the present study is the derivation of a new improved method to measure metallicities from the calcium triplet, which allowed us, and should encourage future works, to extract reasonably accurate information from low  $S/N$  spectra.

Support was provided by NSF (AST-0307931, AST-074979), HST (GO-10265, 10816) and by R.M. Rich. The authors thank Stephen Gwyn for assistance with obtaining the photometry from the CFHT archive. We gratefully acknowledge P. Guhathakurta and J. Kalirai for assisting in the Keck observations. H. Ferguson is thanked for helpful comments. We are also grateful to Marc Davis and the DEEP team, and to Phil Choi and George Helou, for obtaining some of the observations used in this study.

We are grateful to Sandy Faber and the DEIMOS team for building an outstanding instrument and for extensive help and guidance throughout the observing runs. The spec2d data reduction pipeline for DEIMOS was developed at UC Berkeley with support from NSF grant AST-0071048. The staff of the W.M. Keck Observatory, in particular Greg Wirth, is thanked for assistance with observations and data recovery. Data presented herein were obtained using the W. M. Keck Observatory, which is operated as a scientific partnership among Caltech, the University of California, and NASA. The Observatory was made possible by the generous financial support of the W. M. Keck Foundation. This research used the facilities of the Canadian Astronomy Data Centre operated by the National Research Council of Canada with the support of the Canadian Space Agency.

## APPENDIX

### BACKGROUND GALAXIES

In the full sample of DEIMOS targets taken for the entire project, we identified a still large number of  $\sim 400$  galaxies background galaxies, which corresponds to a striking contamination fraction of  $\sim 11\%$ . It is possible that more galaxies were missed during the classification of the spectra and rather flagged as bad quality data, although we verified that no “true” dwarf or giant star was mistaken as a galaxy spectrum and vice versa. These galaxies cover the full color range from  $\sim 0.5$  to  $3.5$  in  $V - i'$ , with the majority falling in the interval between 1 and 2 (see the CMD in Fig. 3). Despite the thorough pre-selection of potential M31 giant candidates on the upper RGB and, for some of the inner fields, using Washington photometry (e.g., Gilbert et al. 2006), the partially poor seeing conditions during the photometric runs (obtained at the KPNO; see Ostheimer 2003; Gilbert et al. 2006) hampered an appropriate *a priori* rejection of non-stellar extragalactic point sources.

For those galaxies identified here, redshifts were measured from the Doppler shifts of generally 2–3 major emission features, such as the Balmer  $H\alpha$ ,  $H\beta$ ,  $H\gamma$  lines, the [O II] 3727Å doublet and/or the [O III] 5007Å line. For rare occasions ( $\sim 5$  of the galaxies) we could also detect the strong Ca H,K features in absorption. The final redshift distribution is displayed in Fig. 20. The first thing to note is that our sample includes a fairly broad range in redshifts, reaching from  $z \sim 0.04$  to  $z \sim 1.35$ .

This distribution should, however, not be taken as representative of the true galaxy distribution in the line of sight towards M31. This is due to our identification criteria based on only a small number of spectral features, which are then redshifted into the limited spectral range of DEIMOS (see also Kirby et al. 2007), biasing the distribution towards only selected redshift intervals. Hence, a detailed derivation of their physical properties and star formation rates has to be beyond the scope of this work and is left for a future paper (Koch et al., in prep.).

## REFERENCES

- Armandroff, T. E., & Zinn, R. 1988, *AJ*, 96, 92  
 Armandroff, T. E., & Da Costa, G. S. 1991, *AJ*, 101, 1329  
 Ashman, K. M., Bird, C. M., & Zepf, S. E. 1994, *AJ*, 108, 2348  
 Battaglia, G., Irwin, M., Tolstoy, E., Hill, V., Helmi, A., Letarte, B., & Jablonka, P. 2008, *MNRAS*, 338, 183  
 Bellazzini, M., Cacciari, C., Federici, L., Fusi Pecci, F., & Rich, M. 2003, *A&A*, 405, 867  
 Bosler, T. L., Smecker-Hane, T. A., & Stetson, P. B. 2007, *MNRAS*, 378, 318  
 Brown, T. M., Ferguson, H. C., Smith, E., Kimble, R. A., Sweigart, A. V., Renzini, A., Rich, R. M., & Vandenberg, D. A. 2003, *ApJ*, 592, L17  
 Brown, T. M., Smith, E., Ferguson, H. C., Rich, R. M., Guhathakurta, P., Renzini, A., Sweigart, A. V., & Kimble, R. A. 2006, *ApJ*, 652, 323  
 Brown, T. M., et al. 2007, *ApJ*, 658, L95  
 Bullock, J. S., & Johnston, K. V. 2005, *ApJ*, 635, 931  
 Carney, B. W., Laird, J. B., Latham, D. W., & Aguilar, L. A. 1996, *AJ*, 112, 668  
 Carollo, D., et al. 2007, *Nature*, 450, 1020  
 Carrera, R., Gallart, C., Pancino, E., & Zinn, R. 2007, *AJ*, 134, 1298  
 Carretta, E., & Gratton, R. 1997, *A&AS*, 121, 95  
 Cenarro, A. J., Cardiel, N., Gorgas, J., Peletier, R. F., Vazdekis, A., & Prada, F. 2001, *MNRAS*, 326, 959  
 Chapman, S. C., Ibata, R., Lewis, G. F., Ferguson, A. M. N., Irwin, M., McConnachie, A., & Tanvir, N. 2006, *ApJ*, 653, 255  
 Chapman, S. C., et al. 2008, *MNRAS*, submitted  
 Chiba, M., & Beers, T. C. 2000, *AJ*, 119, 2843  
 Cole, A. A., Smecker-Hane, T. A., Tolstoy, E., Bosler, T. L., & Gallagher, J. S. 2004, *MNRAS*, 347, 367  
 Durrell, P. R., Harris, W. E., & Pritchett, C. J. 2001, *AJ*, 121, 2557  
 Fardal, M. A., Babul, A., Geehan, J. J., & Guhathakurta, P. 2006, *MNRAS*, 366, 1012  
 Fardal, M. A., Guhathakurta, P., Babul, A., & McConnachie, A. W. 2007, *MNRAS*, 380, 15  
 Ferguson, A. M. N., Irwin, M. J., Ibata, R. A., Lewis, G. F., & Tanvir, N. R. 2002, *AJ*, 124, 1452  
 Ferguson, A. M. N., Johnson, R. A., Faria, D. C., Irwin, M. J., Ibata, R. A., Johnston, K. V., Lewis, G. F., & Tanvir, N. R. 2005, *ApJ*, 622, L109  
 Font, A. S., Johnston, K. V., Bullock, J. S., & Robertson, B. E. 2006, *ApJ*, 646, 886  
 Gallart, C., Zoccali, M., & Aparicio, A. 2005, *ARA&A*, 43, 387  
 Galletti, S., Bellazzini, M., & Ferraro, F. R. 2004, *A&A*, 423, 925  
 Garnavich, P. M., Vandenberg, D. A., Zurek, D. R., & Hesser, J. E. 1994, *AJ*, 107, 1097  
 Gilbert, K. M., et al. 2006, *ApJ*, 652, 1188  
 Gilbert, K. M., et al. 2007, *ApJ*, 668, 245  
 Guhathakurta, P., et al. 2006, *AJ*, submitted (astro-ph/0502366)

- Guhathakurta, P., et al. 2006, *AJ*, 131, 2497
- Gwyn, S. D. J. 2008, *PASP*, 120, 212
- Helmi, A., et al. 2006, *ApJ*, 651, L121
- Holland, S., Fahlman, G. G., & Richer, H. B. 1996, *AJ*, 112, 1035
- Ibata, R., Irwin, M., Lewis, G., Ferguson, A. M. N., & Tanvir, N. 2001, *Nature*, 412, 49
- Ibata, R., Chapman, S., Ferguson, A. M. N., Irwin, M., Lewis, G., & McConnachie, A. 2004, *MNRAS*, 351, 117
- Ibata, R., Chapman, S., Ferguson, A. M. N., Lewis, G., Irwin, M., & Tanvir, N. 2005, *ApJ*, 634, 287
- Ibata, R., Martin, N. F., Irwin, M., Chapman, S., Ferguson, A. M. N., Lewis, G. F., & McConnachie, A. W. 2007, *ApJ*, 671, 1591
- Irwin, M. J., Ferguson, A. M. N., Ibata, R. A., Lewis, G. F., & Tanvir, N. R. 2005, *ApJ*, 628, L105
- Jones, J. B., Gilmore, G., & Wyse, R. F. G. 1996, *MNRAS*, 278, 146
- Jørgensen, U. G., Carlsson, M., & Johnson, H. R. 1992, *A&A*, 254, 258
- Kalirai, J. S., et al. 2006a, *ApJ*, 648, 389
- Kalirai, J. S., Guhathakurta, P., Gilbert, K. M., Reitzel, D. B., Majewski, S. R., Rich, R. M., & Cooper, M. C. 2006b, *ApJ*, 641, 268
- Kirby, E. N., Guhathakurta, P., Faber, S. M., Koo, D. C., Weiner, B. J., & Cooper, M. C. 2007, *ApJ*, 660, 62
- Kirby, E. N., Guhathakurta, P., & Sneden, C. 2008, *ApJ*, in press (astro-ph/0804.3590)
- Koch, A., & Grebel, E. K. 2006, *AJ*, 131, 1405
- Koch, A., Grebel, E. K., Wyse, R. F. G., Kleyna, J. T., Wilkinson, M. I., Harbeck, D. R., Gilmore, G. F., & Evans, N. W. 2006, *AJ*, 131, 895
- Koch, A., Kleyna, J. T., Wilkinson, M. I., Grebel, E. K., Gilmore, G. F., Evans, N. W., Wyse, R. F. G., & Harbeck, D. R. 2007, *AJ*, 134, 566
- Koch, A., Grebel, E. K., Gilmore, G. F., Wyse, R. F. G., Kleyna, J. T., Harbeck, D. R., Wilkinson, M. I., & Wyn Evans, N. 2008, *AJ*, 135, 1580
- Kuijken, K., & Dubinski, J. 1995, *MNRAS*, 277, 1341
- Majewski, S. R., Ostheimer, J. C., Patterson, R. J., Kunkel, W. E., Johnston, K. V., & Geisler, D. 2000, *AJ*, 119, 760
- Majewski, S. R., et al. 2004, *AJ*, 128, 245
- Majewski, S. R., et al. 2007, *ApJ*, 670, L9
- Marigo, P., Girardi, L., Bressan, A., Groenewegen, M. A. T., Silva, L., & Granato, G. L. 2008, *A&A*, 482, 883
- Martin, N. F., Irwin, M. J., Ibata, R. A., Conn, B. C., Lewis, G. F., Bellazzini, M., Chapman, S., & Tanvir, N. 2006a, *MNRAS*, 367, L69
- Martin, N. F., Ibata, R. A., Irwin, M. J., Chapman, S., Lewis, G. F., Ferguson, A. M. N., Tanvir, N., & McConnachie, A. W. 2006b, *MNRAS*, 371, 1983
- Martin, N. F., Ibata, R. A., & Irwin, M. 2007, *ApJ*, 668, L123
- McConnachie, A. W., Irwin, M. J., Ferguson, A. M. N., Ibata, R. A., Lewis, G. F., & Tanvir, N. 2005, *MNRAS*, 356, 979
- McConnachie, A. W., Chapman, S. C., Ibata, R. A., Ferguson, A. M. N., Irwin, M. J., Lewis, G. F., Tanvir, N. R., & Martin, N. 2006, *ApJ*, 647, L25
- Merrifield, M. R., & Kuijken, K. 1998, *MNRAS*, 297, 1292
- Mori, M., & Rich, R. M. 2008, *ApJ*, 674, L77
- Mouhcine, M., Ferguson, H. C., Rich, R. M., Brown, T. M., & Smith, T. E. 2005, *ApJ*, 633, 821
- Mould, J., & Kristian, J. 1986, *ApJ*, 305, 591
- O'Connell, R. W. 1973, *AJ*, 78, 1074
- Ostheimer, J. C. J. 2003, Ph.D. Thesis, University of Virginia
- Palma, C., Majewski, S. R., Siegel, M. H., Patterson, R. J., Ostheimer, J. C., & Link, R. 2003, *AJ*, 125, 1352
- Pasquini, L., et al. 2002, *The Messenger*, 110, 1
- Peñarrubia, J., McConnachie, A., & Babul, A. 2006, *ApJ*, 650, L33
- Pritchett, C. J., & van den Bergh, S. 1994, *AJ*, 107, 1730
- Reitzel, D. B., & Guhathakurta, P. 2002, *AJ*, 124, 234
- Rich, R. M., Mighell, K. J., Freedman, W. L., & Neill, J. D. 1996, *AJ*, 111, 768
- Rich, R. M., Corsi, C. E., Cacciari, C., Federici, L., Fusi Pecci, F., Djorgovski, S. G., & Freedman, W. L. 2005, *AJ*, 129, 2670
- Robin, A. C., Reylé, C., Derrière, S., & Picaud, S. 2003, *A&A*, 409, 523
- Rocha-Pinto, H. J., Majewski, S. R., Skrutskie, M. F., Crane, J. D., & Patterson, R. J. 2004, *ApJ*, 615, 732
- Rutledge, G. A., Hesser, J. E., & Stetson, P. A., Mateo, M., Simard, L., Bolte, M., Friel, E. D., & Copin, Y. 1997a, *PASP*, 109, 883
- Rutledge, G. A., Hesser, J. E., & Stetson, P. A., 1997b *PASP*, 109, 907
- Schiavon, R. P., Barbuy, B., Rossi, S. C. F., & Milone, A. 1997, *ApJ*, 479, 902
- Schlegel, D. J., Finkbeiner, D. P., & Davis, M. 1998, *ApJ*, 500, 525
- Sherwin, B. D., Loeb, A., & O'Leary, R. M. 2008, *MNRAS*, 386, 1179
- Simon, J. D., & Geha, M. 2007, *ApJ*, 669, 327
- Smith, G., & Drake, J. J. 1990, *A&A*, 231, 125
- Stanek, K. Z., & Garnavich, P. M. 1998, *ApJ*, 503, L131
- Tonry, J. L., & Davis, M. 1979, *AJ*, 84, 1511
- Widrow, L. M., Perrett, K. M., & Suyu, S. H. 2003, *ApJ*, 588, 311



TABLE 1  
DEIMOS MASK OBSERVATION DETAILS

Mask	Date of observation	P.I.	Projected radius <sup>a</sup> [kpc]	Mask center (J2000.0)		P.A. [degree]
Minor axis fields						
f109_1	2005 Aug 29	Rich	9 (194)	00 45 47.06	+40 56 52.3	23.9
H11_1	2004 Sep 20	Rich	12 (190)	00 46 21.94	+40 41 42.7	21.0
H11_2	2004 Sep 20	Rich	12 (190)	00 46 20.57	+40 41 41.9	-21.0
f116_1	2005 Aug 28	Rich	13 (189)	00 46 54.63	+40 41 33.3	22.6
f115_1	2005 Aug 28	Rich	14 (188)	00 47 32.51	+40 42 05.3	-20.0
f123_1	2005 Aug 28	Rich	17 (185)	00 48 05.79	+40 29 35.5	-20.0
f135_1	2005 Aug 29	Rich	17 (186)	00 46 25.22	+40 11 45.1	-27.0
f130_3	2006 Nov 22	Guhathakurta	19 (182)	00 48 35.01	+40 16 01.2	90.0
f130_1	2005 Aug 28	Rich	22 (180)	00 49 11.59	+40 11 51.9	-20.0
f130_2	2006 Nov 21	Guhathakurta	22 (180)	00 49 38.44	+40 16 04.8	90.0
a0_3	2004 Jun 17	Helou	29 (175)	00 51 50.65	+40 07 05.9	0.0
a0_1	2002 Aug 16	Rich	31 (172)	00 51 51.04	+39 50 24.9	-17.9
a0_2	2002 Oct 12	Rich	31 (172)	00 51 30.49	+39 44 02.3	90.0
mask4	2006 Nov 22	Guhathakurta	37 (166)	00 54 08.84	+39 41 47.0	172.0
123Glo	2005 Oct 01	Chapman	60 (143)	00 58 20.30	+38 01 46.0	147.0
124Glo	2005 Oct 02	Chapman	60 (143)	00 58 07.47	+38 05 00.9	147.0
m6_1	2003 Oct 01	Rich	87 (119)	01 09 51.88	+37 47 04.4	0.0
m6_2	2005 Jun 09	Helou	87 (118)	01 08 36.22	+37 29 04.6	0.0
m8_1	2005 Jul 07	Davis	118 (90)	01 18 12.17	+36 16 13.1	0.0
m8_2	2005 Jul 07	Davis	119 (89)	01 18 35.63	+36 14 31.4	0.0
m11_2	2003 Sep 30	Rich	159 (54)	01 29 33.57	+34 27 56.5	0.0
m11_1	2003 Oct 01	Rich	162 (51)	01 29 34.48	+34 13 49.8	0.0
m11_3	2005 Jul 08	Davis	162 (51)	01 30 02.38	+34 13 31.7	0.0
m11_4	2005 Jul 08	Davis	164 (50)	01 30 37.34	+34 13 17.1	0.0
Off axis spheroid fields						
H13s_1	2004 Sept 20	Rich	21 (186)	00 44 15.14	+39 44 23.5	21.0
H13s_2	2004 Sept 20	Rich	21 (186)	00 44 14.72	+39 44 23.4	-21.0
a3_2	2002 Oct 11	Rich	32 (173)	00 47 47.30	+39 06 03.4	178.2
a3_3	2002 Oct 26	Rich	32 (173)	00 48 22.81	+39 12 38.4	270.0
a3_1	2002 Aug 16	Rich	34 (171)	00 48 21.69	+39 02 38.0	64.2
a13_3	2005 Nov 05	Guhathakurta	57 (171)	00 42 25.86	+37 08 28.8	0.0
a13_4	2005 Nov 05	Guhathakurta	57 (173)	00 41 32.55	+37 08 44.6	0.0
a13_1	2003 Sept 30	Rich	59 (168)	00 42 58.20	+36 59 04.7	0.0
a13_2	2003 Sept 30	Rich	61 (171)	00 41 30.07	+36 50 15.7	0.0
a19_1	2005 Aug 29	Rich	81 (173)	00 38 15.77	+35 28 07.7	90
b15_3	2005 Sept 07	Guhathakurta	94 (129)	00 53 36.91	+34 50 13.6	-90.0
b15_1	2005 Sept 07	Guhathakurta	96 (129)	00 53 23.41	+34 37 17.1	-90.0

<sup>a</sup> Numbers in parentheses are projected distances from M33.

TABLE 2  
NUMBER OF RELIABLE MEASUREMENTS PER MASK

Mask	# Targets on mask	# Reliable velocities <sup>a</sup>	# M31 giant candidates	# M31 giants with Metallicities $(V - i') \leq 2$	# M31 giants with Metallicities $(V - i') > 2$	# Expected blue dwarfs <sup>b</sup>
f109_1	204	186	158	105	4	1
H11_1	139	102	85	58	5	1
H11_2	140	115	93	53	5	1
f116_1	139	116	98	59	5	1
f115_1	187	162	121	87	4	1
f123_1	138	112	83	62	4	1
f135_1	146	123	92	73	2	1
f130_3	70	41	29	38	1	0
f130_1	112	88	44	24	2	1
f130_2	109	75	34	11	1	1
a0_3	93	65	36	24	1	1
a0_1	90	44	28	17	3	1
a0_2	93	47	31	15	0	1
mask4	101	60	18	15	0	2
123Glo	103	91	13	5	4	3
124Glo	105	102	16	8	6	3
m6_1	79	39	12	5	1	1
m6_2	75	27	7	5	0	1
m8_1	62	20	2	2	0	1
m8_2	65	25	5	3	0	1
m11_2	72	22	2	1	0	1
m11_1	74	35	8	5	0	1
m11_3	85	27	1	1	0	1
m11_4	82	31	5	3	0	1
H13s_1	134	106	92	52	5	0
H13s_2	100	75	52	30	4	1
a3_2	80	30	18	9	1	1
a3_3	87	47	32	13	4	1
a3_1	86	30	24	7	1	0
a13_3	113	37	16	11	1	1
a13_4	90	34	12	7	0	1
a13_1	84	31	16	11	0	0
a13_2	74	27	14	11	0	0
a19_1	76	37	6	3	0	1
b15_3	76	32	10	6	0	1
b15_1	68	21	4	4	0	0

NOTE. — The listed number of velocity and metallicity measurements excludes “serendipitous” extractions and background galaxies.

<sup>a</sup> Prior to the membership separation.

<sup>b</sup> Based on the comparison with the Besançon model. See text for details.

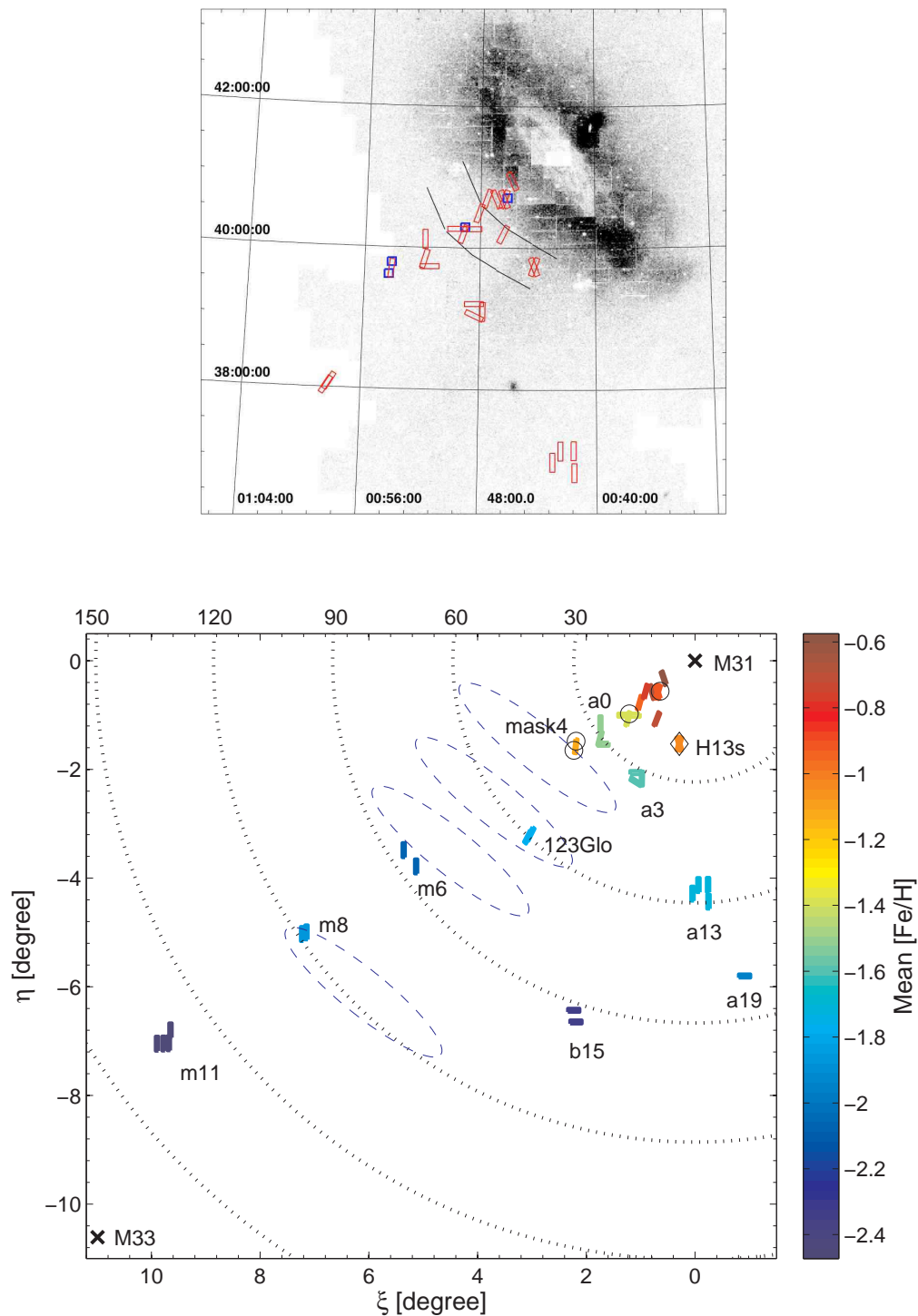


FIG. 1.— Top panel: Location of the targeted inner fields (red rectangles) on a star count map of M31 (courtesy of M. Irwin). Shown as blue squares are the HST fields of Brown et al. (2003, 2006, 2007). The solid black lines delineate the region in which we detect a break in the abundance profile (see Figs. 14–16) – this transition occurs remarkably close to the edge of the perturbed disk component in the star count maps. Bottom panel: Representation of the full data set in standard coordinates. Numbers at the top denote projected distances from M31 in kpc, also indicated by dashed circles. The individual masks are color coded by their metallicity (see Sect. 7). The black diamond represents the stream field H13s (Kalirai et al. 2006b), black circles are the HST fields, and M31 and M33 are indicated as crosses. Dashed ellipses illustrate the approximate location of the tangential streams found in the Ibata et al. (2007) maps.

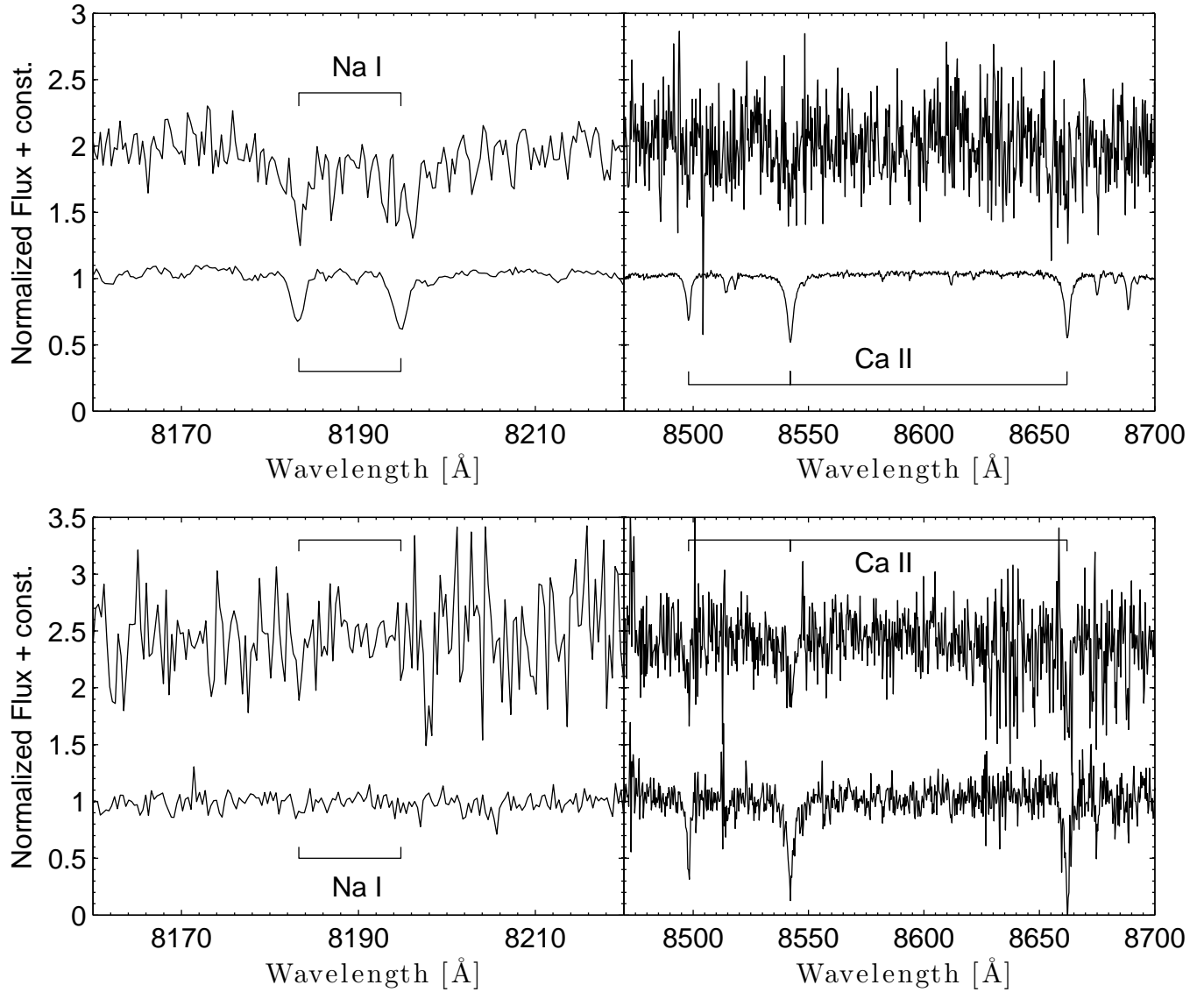


FIG. 2.— Sample spectra of foreground dwarfs (top panel) and M31 red giants (bottom panel) with low and higher  $S/N$  ratios. The low  $S/N$  data ( $S/N=6$  and  $8$ ) represent the approximate limit for which velocities and CaT metallicities could be barely determined; the  $S/N$  for the higher quality spectra are  $\sim 120$  (top) and  $\sim 20$  (bottom). Indicated are the wavelength regions of the surface gravity sensitive sodium doublet and the CaT.

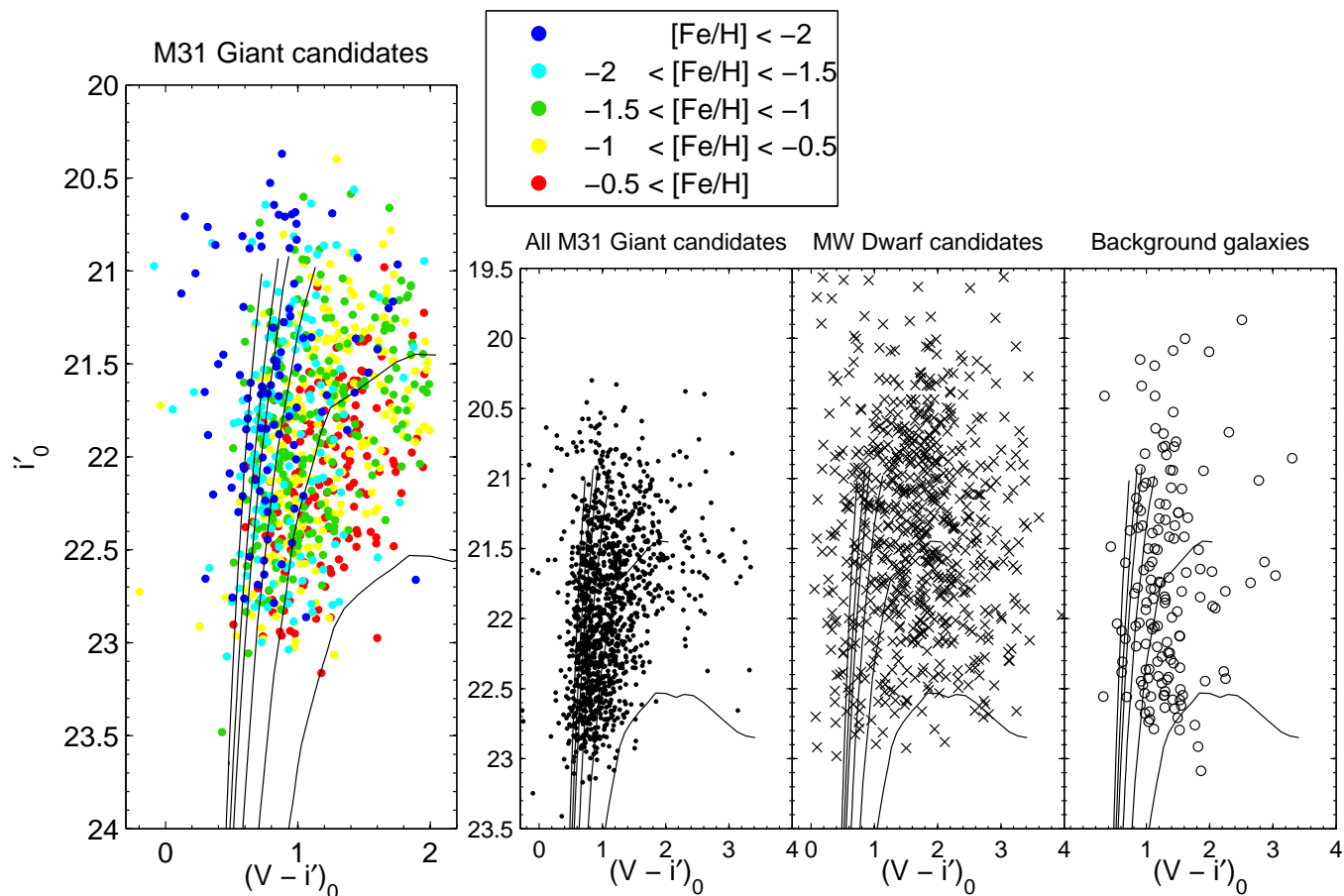


FIG. 3.— Color magnitude diagrams of target objects, separated into M31 giants, foreground dwarfs and background galaxy contamination. Giant candidates for which we could determine spectroscopic metallicities are color coded by their  $[\text{Fe}/\text{H}]_{\text{CAT}}$  in the leftmost panel. The small numbers of metal poor giants that are plotted to lie to the blue of the bluest isochrone were carefully vetted and pass as likely M31 giants. If these stars are excluded from the sample, our conclusions are not affected. The solid lines are isochrone sets of Girardi et al. (2002) for an age of 12.7 Gyr and metallicities  $[M/H]$  of (left to right)  $-2.3$ ,  $-1.7$ ,  $-1.4$ ,  $-1.0$ ,  $-0.5$ , and  $0.0$ .

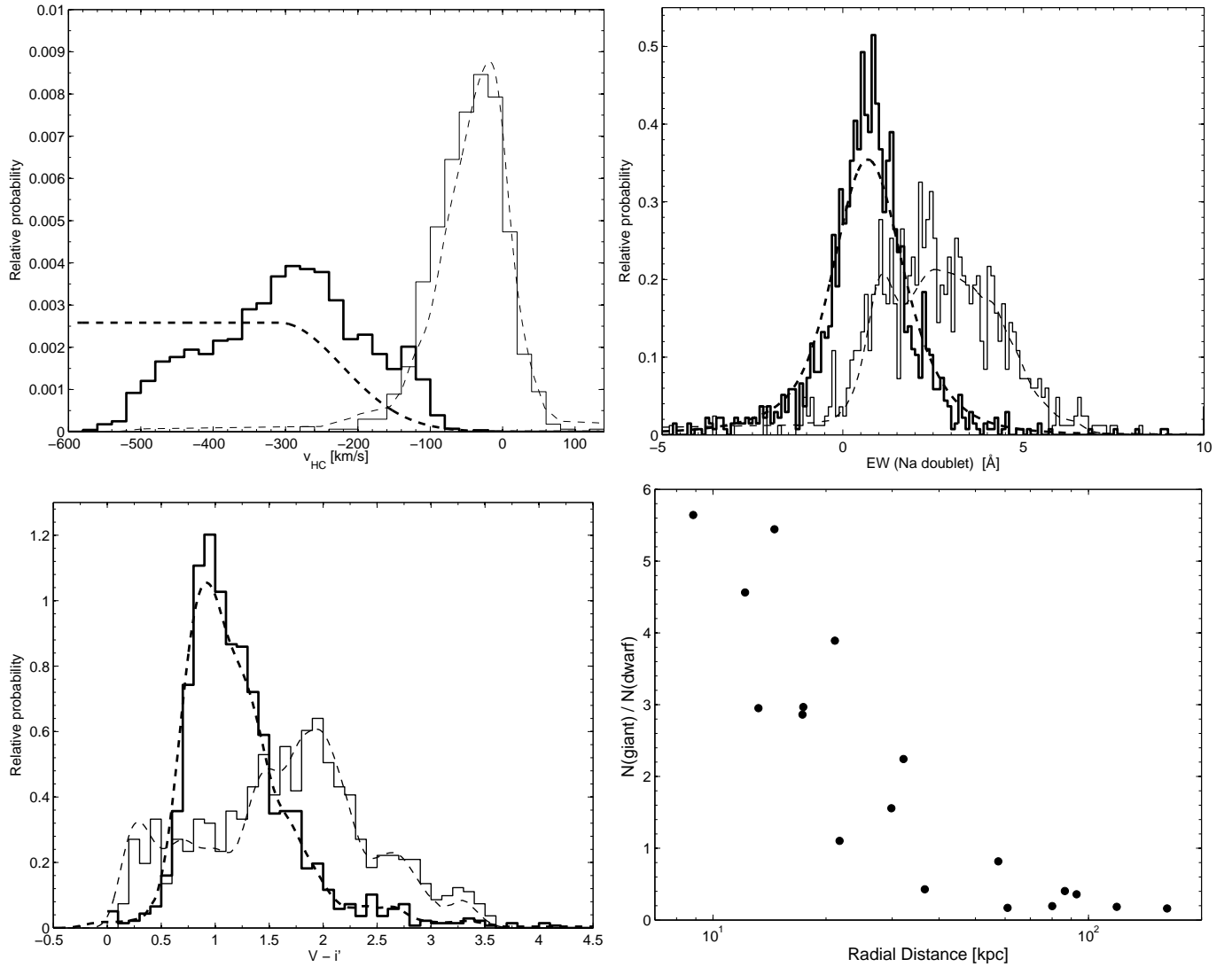


FIG. 4.— Probability distributions (PDFs) for those parameters that we used as criteria for dwarf/giant separation, i.e., Na doublet EW,  $V - i'$  color and radial velocity. The dashed lines each indicate the empirical PDFs defined by the full training samples, while the solid histograms were separated by applying the respective criteria to our full data. Thin and thick lines discriminate between dwarf and giant samples, respectively. Despite a considerable overlap in each individual indicator, the statistical combination of all three pieces of information allows for an efficient dwarf removal. The bottom right panel shows the ratio of thus separated giant to dwarf stars, separately for each field. See text for details.

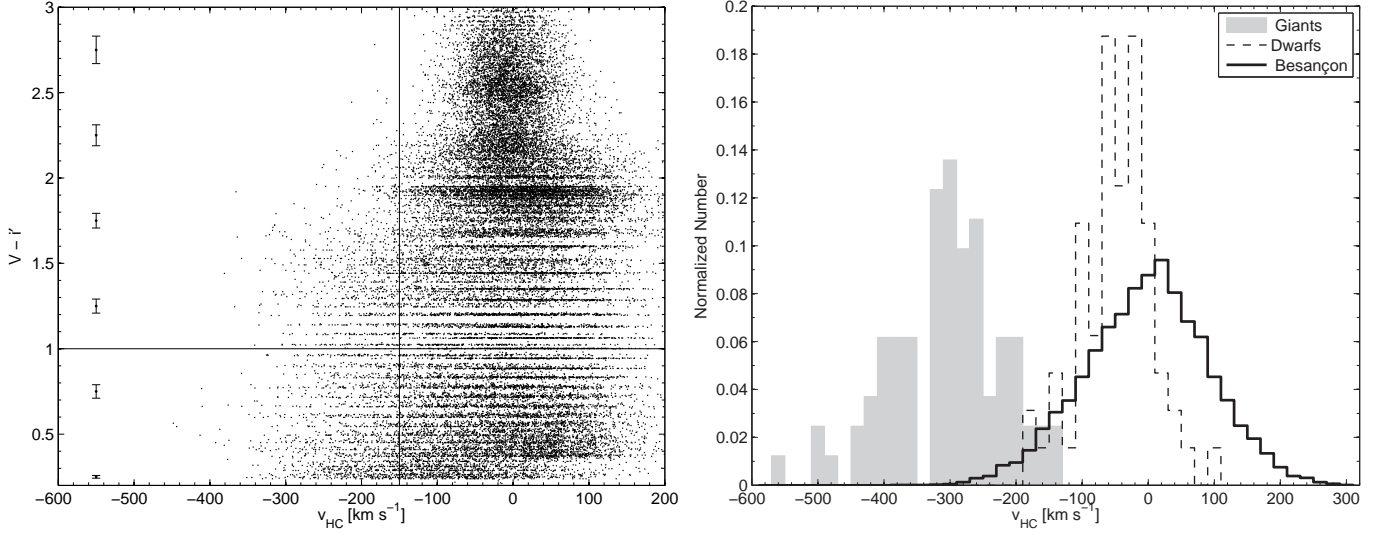


FIG. 5.— Left panel: Color-velocity distribution of foreground dwarfs from the Galactic Besançon model (Robin et al. 2003), at a projected distance of 160 kpc to M31. The solid lines illustrate the cuts we used to assess the number of undetectable blue dwarfs in our M31 giant sample. Also indicated are the observed photometric errors. The right panel shows velocity distributions of our observed stars (shaded and dashed histograms) with  $V - r' \leq 1$  and the expected blue dwarfs from the Besançon model (solid histogram). The fraction of unresolvable blue dwarfs in our giant sample is well below 3% and negligible.

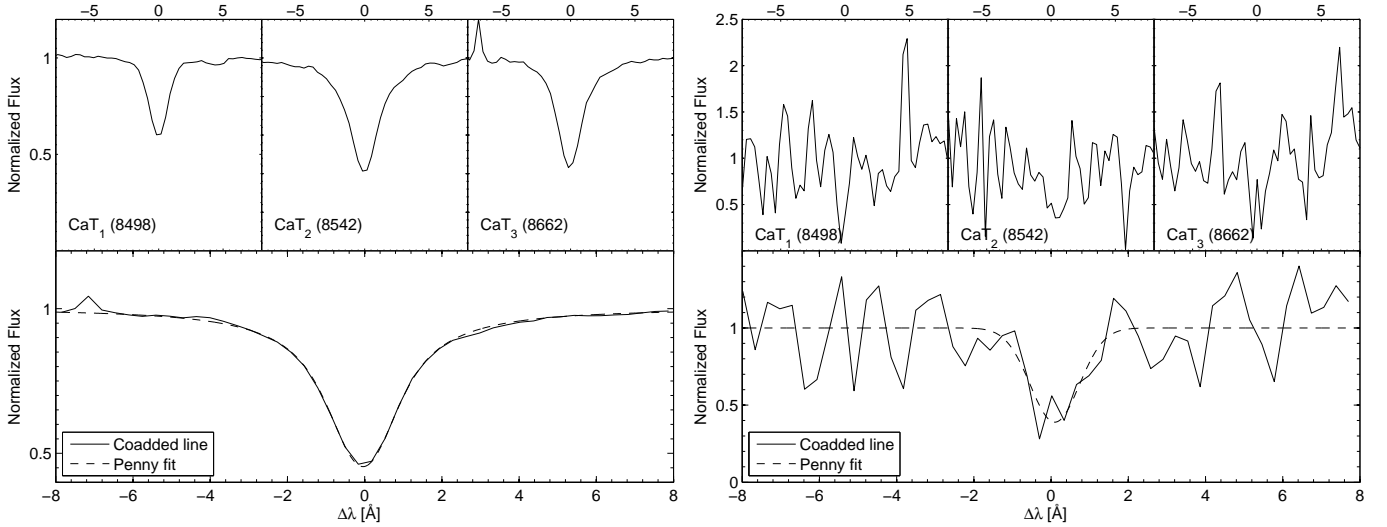


FIG. 6.— Illustration of the CaT condition in a high  $S/N$  spectrum of a red giant in a calibration globular cluster (star N3201-S11;  $S/N \sim 110$ ;  $V = 14.5$  mag;  $v_{\text{HC}} = 485$  km s $^{-1}$ ;  $\langle \Sigma W \rangle = 3.8 \text{\AA}$ ) and a low  $S/N$  DEIMOS spectrum of a M31 red giant (star 5004266;  $S/N \sim 4$ ;  $V = 21.7$  mag;  $v_{\text{HC}} = -338$  km s $^{-1}$ ;  $\langle \Sigma W \rangle = 2.4 \text{\AA}$ ). The top panels display each individual Ca line, shifted to a common line center, and the bottom panels show the weighted coadded line (solid line), from which we measure the CaT line strengths using a Penny (i.e., Gaussian plus Lorentz profile) fit (dashed line).

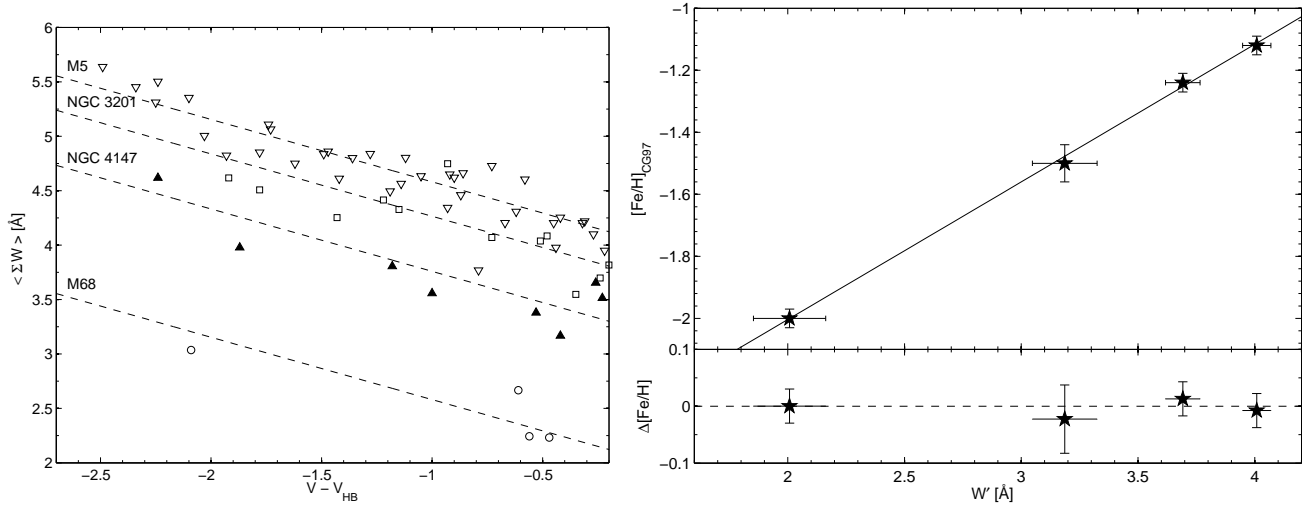


FIG. 7.— Left Panel: Linestrengths of red giants in the calibration clusters from FLAMES data (Koch et al. 2006) vs. magnitude above the horizontal branch. The right panel shows the metallicities of these globular clusters on the scale of Carretta & Gratton (1997), with the residuals of the best-fit relation (eq. 6) at the bottom. Solid and dashed lines indicate these best-fit calibrations (eqs. 5,6). All these measurements are based on the coadded CaT.

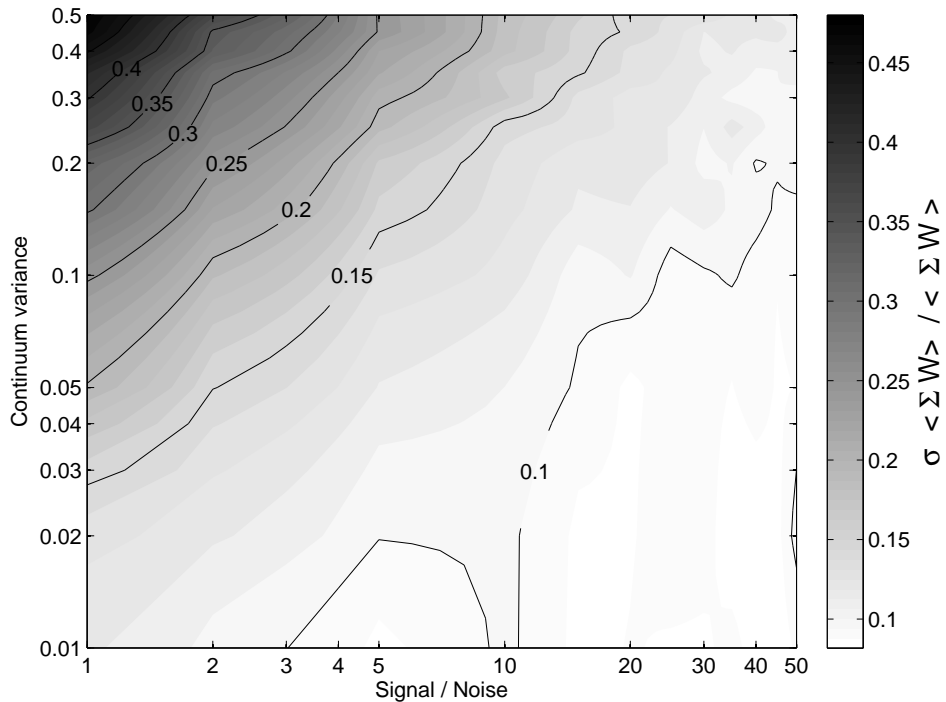


FIG. 8.— Distribution of the relative error on the measured coadded line strength  $\langle \Sigma W \rangle$ , determined from Monte Carlo simulations, as a function of spectral quality. For our observed spectra, these values are propagated through Eqs. 5,6 to obtain the spectroscopic metallicity uncertainty.



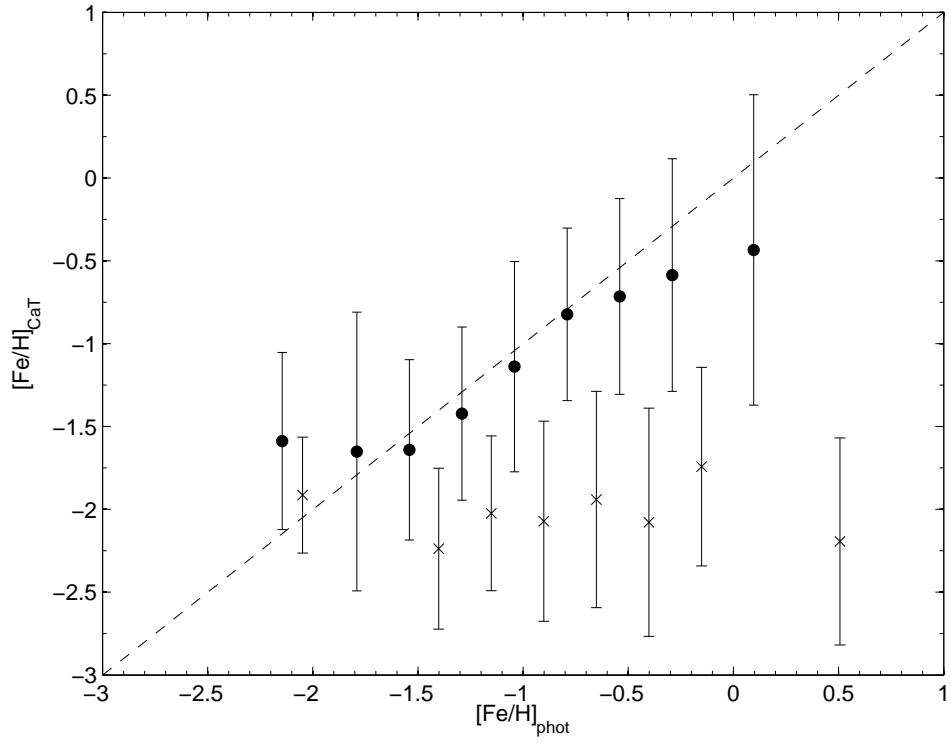


FIG. 9.— Spectroscopic versus photometric metallicities for dwarf (crosses) and giant (points) candidates. Shown each are mean and  $1\sigma$  scatter. The dwarf stars clearly deviate from unity (solid line). Data were binned by 0.25 dex except for the most metal poor and metal rich bin, where we chose to include 20 stars for better sampling.

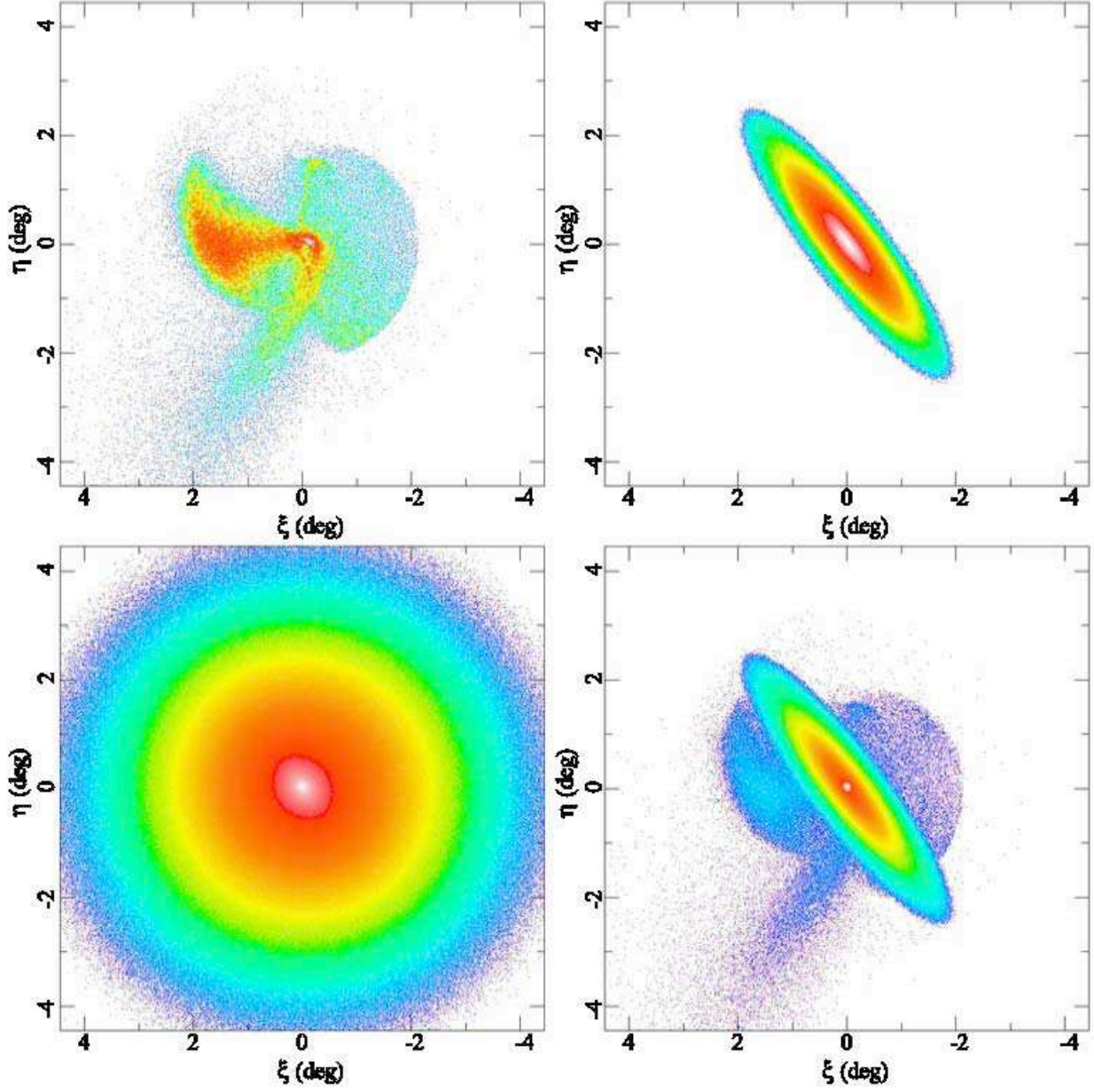


FIG. 10.— Snapshot of the simulation data at 1 Gyr in standard coordinates and color-coded by the particle density (Mori & Rich 2008). Each subpanel separately displays a different component: the accreted satellite only (top left), disk and bulge (top right), spherical halo (bottom left), and disk, bulge plus satellite (bottom right).

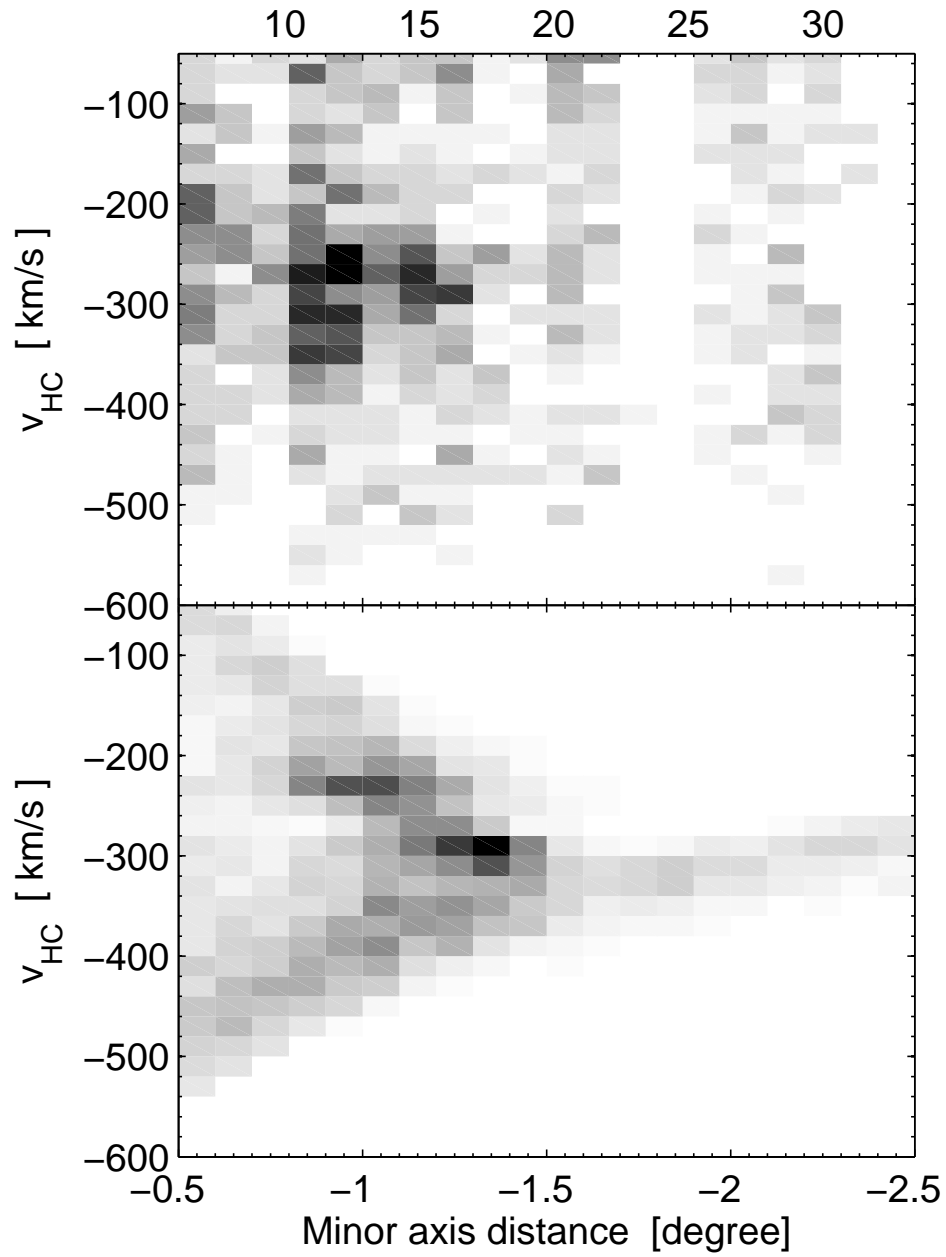


FIG. 11.— Density distribution (with arbitrary scaling) of radial velocities along the minor axis. The top panel displays our observed minor axis data within 35 kpc, whereas the bottom panel shows the distribution of the satellite particles from our simulation. Numbers at the top indicate distances in kpc to guide the eye.

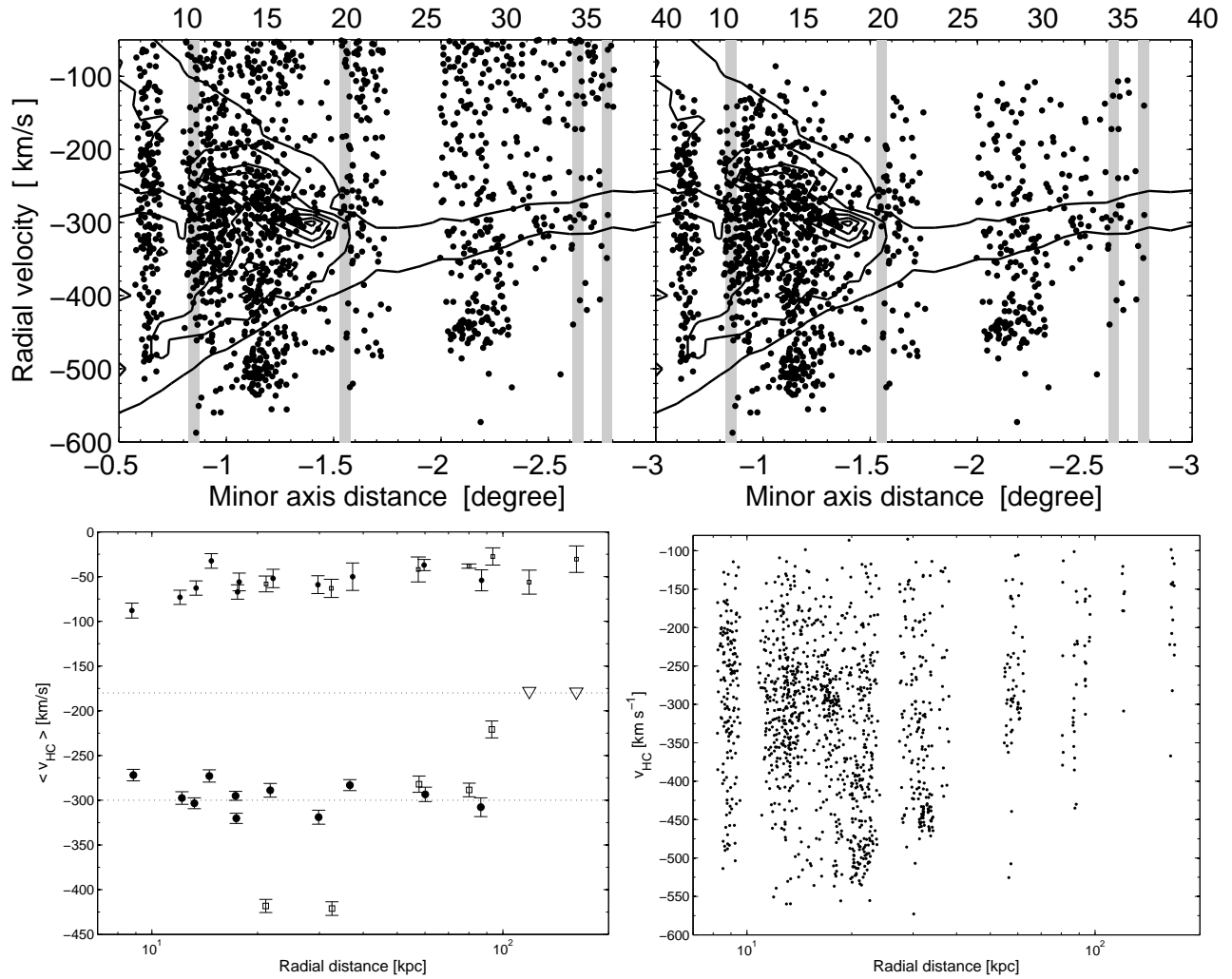


FIG. 12.— Top panel: Radial velocities as a function of radial distance along the minor axis. Shown left is the the complete spectroscopic sample, without the removal of foreground dwarfs, within the inner 40 kpc, while the data shown in the right panel have been cleared of the foreground contamination using the methods described in Sect. 4. Indicated as grey shaded bars are the HST fields of Brown et al. (2003; 2006; 2007). The black contours delineate the distribution from our simulations (see Fig. 11, bottom panel). Numbers at the top indicate distances in kpc to guide the eye. The bottom left panel shows the radial variation of *mean* radial velocity for minor-axis (filled circles) and off-axis (open squares) fields. Small symbols at  $v_{\text{HC}} \sim -50 \text{ km s}^{-1}$  are for the dwarf stars, while the larger symbols below  $-180 \text{ km s}^{-1}$  show the giant distributions. Comparison with the dotted lines at the systemic velocities of M31 ( $-300 \text{ km s}^{-1}$ ) and M33 ( $-180 \text{ km s}^{-1}$ ) suggests that the giant samples in the outermost two fields appear to be suffering from contamination by M33 members (see also Fig. 19). The bottom right panel then shows the distribution of velocities for the full, dwarf-cleaned sample. The stream fields (a3, H13s) reflect in the peaks below  $-400 \text{ km s}^{-1}$  and the peak at  $-520 \text{ km s}^{-1}$ , both of which are reproduced by the simple orbit model of Ibata et al. (2004).

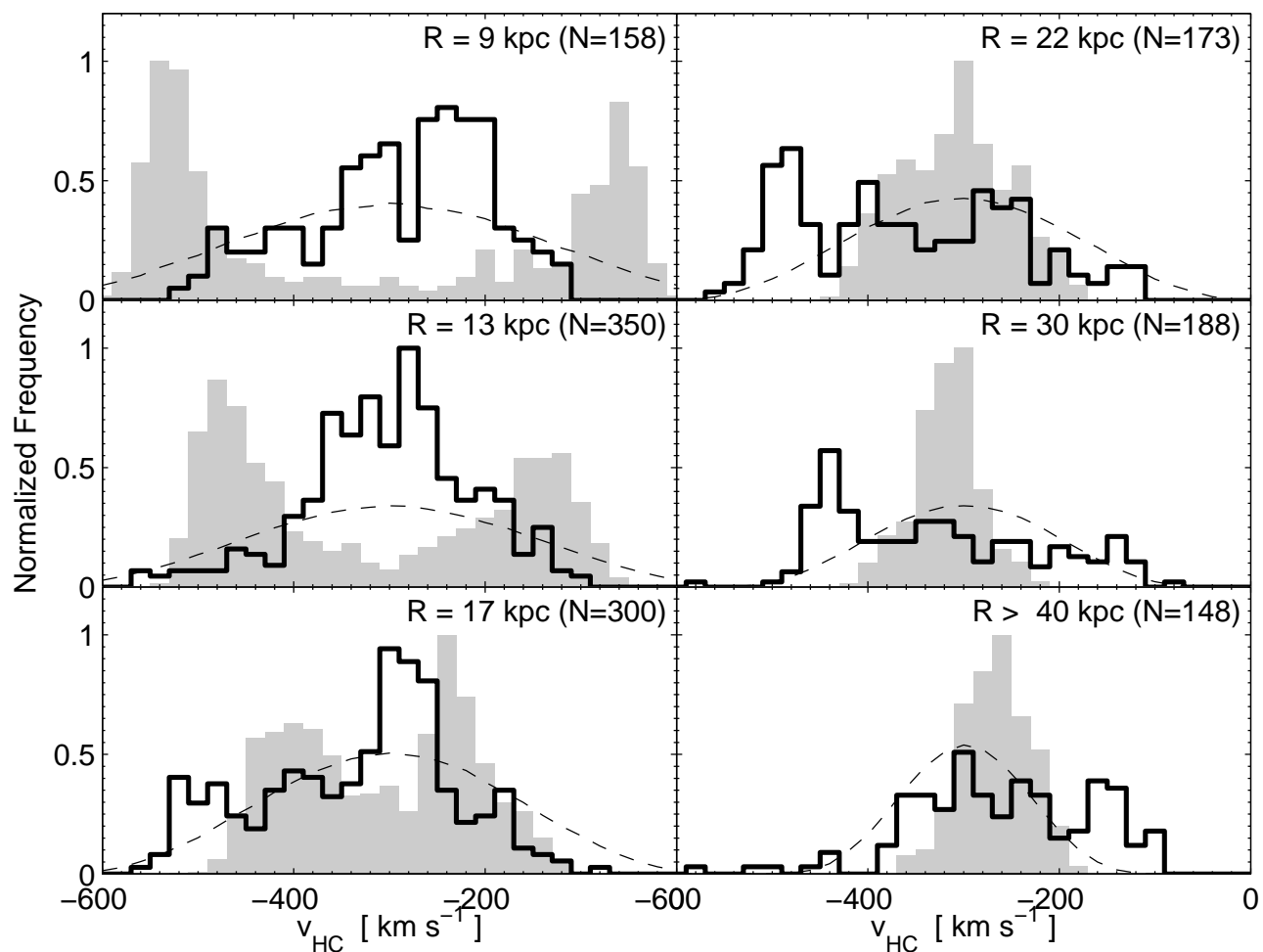


FIG. 13.— Velocity histograms along different radial bins (with the numbers representing their mean locations). The solid line represents our observed, dwarf-cleaned velocity sample. Shown as a shaded histogram is the velocity distribution of the stream particles drawn from our simulations at the same radial location as the observed fields, while the dashed thin line indicates the simulated contribution of M31 halo particles to the velocity structures at these distances. Each distribution has been normalized to unity.

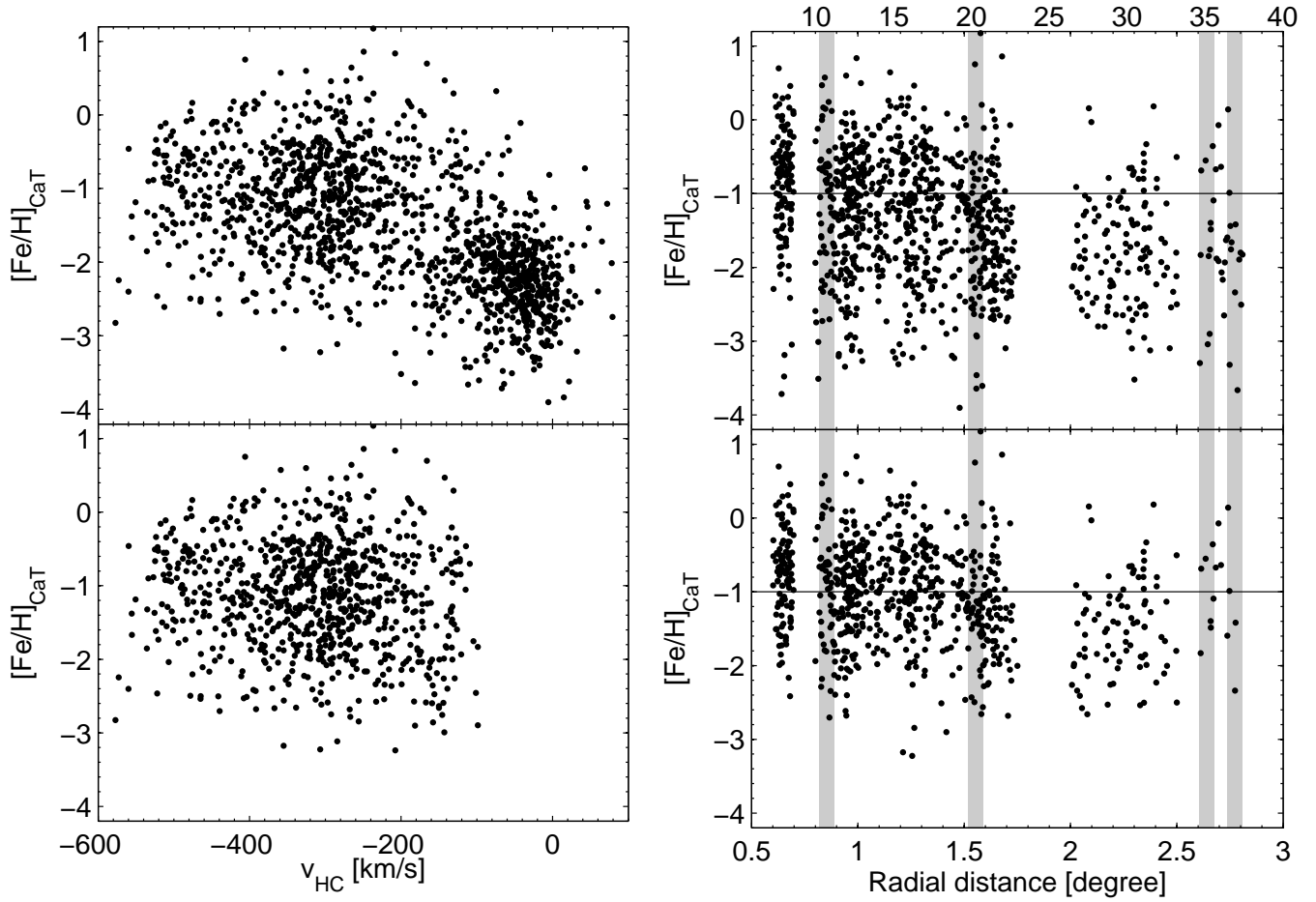


FIG. 14.— Left panels: Spectroscopic metallicity (on the scale of Carretta & Gratton 1997) versus radial velocity. Right panels: the same metallicities within 40 kpc as a function of radial distance. The dwarf contamination clearly stands out as a clump around  $-2$  dex above  $\gtrsim -150$   $\text{km s}^{-1}$ . The top (bottom) panels each display the data set before (after) removal of this contamination. Shaded regions indicate the HST fields of Brown et al. (2003, 2006, 2007). For distributions of all metallicities out to 160 kpc see Fig. 15 (bottom panel). A solid line in the right panel has been added at  $[\text{Fe}/\text{H}]_{\text{CaT}} = -1$  for reference.

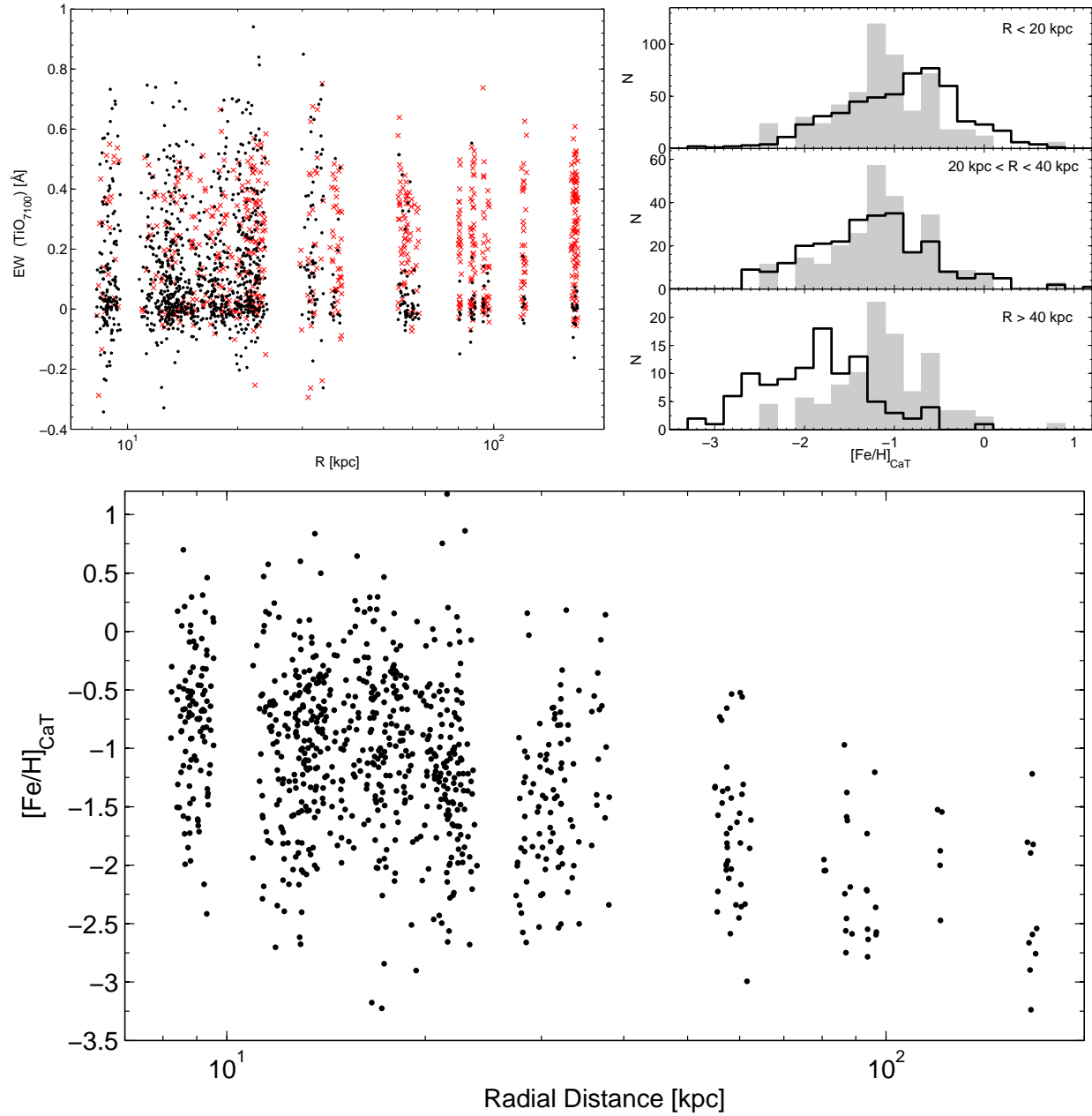


FIG. 15.— A strong abundance gradient is qualitatively already visible in the top left panel, which shows the strength of the TiO band at 7100Å in our entire giant sample (black points) versus radial distance. Note that dwarfs (red crosses) cover the full range in TiO strengths at all radii. The radial metallicity gradient is then clearly present in the spectroscopic MDFs in 3 different radial bins (Top right panel; solid lines) and for our dwarf-cleaned CaT sample (bottom panel). However, none of the distributions fully resembles the stream component (shown as shaded histogram). Notice that there are no metal rich stars beyond  $\sim 50$  kpc.

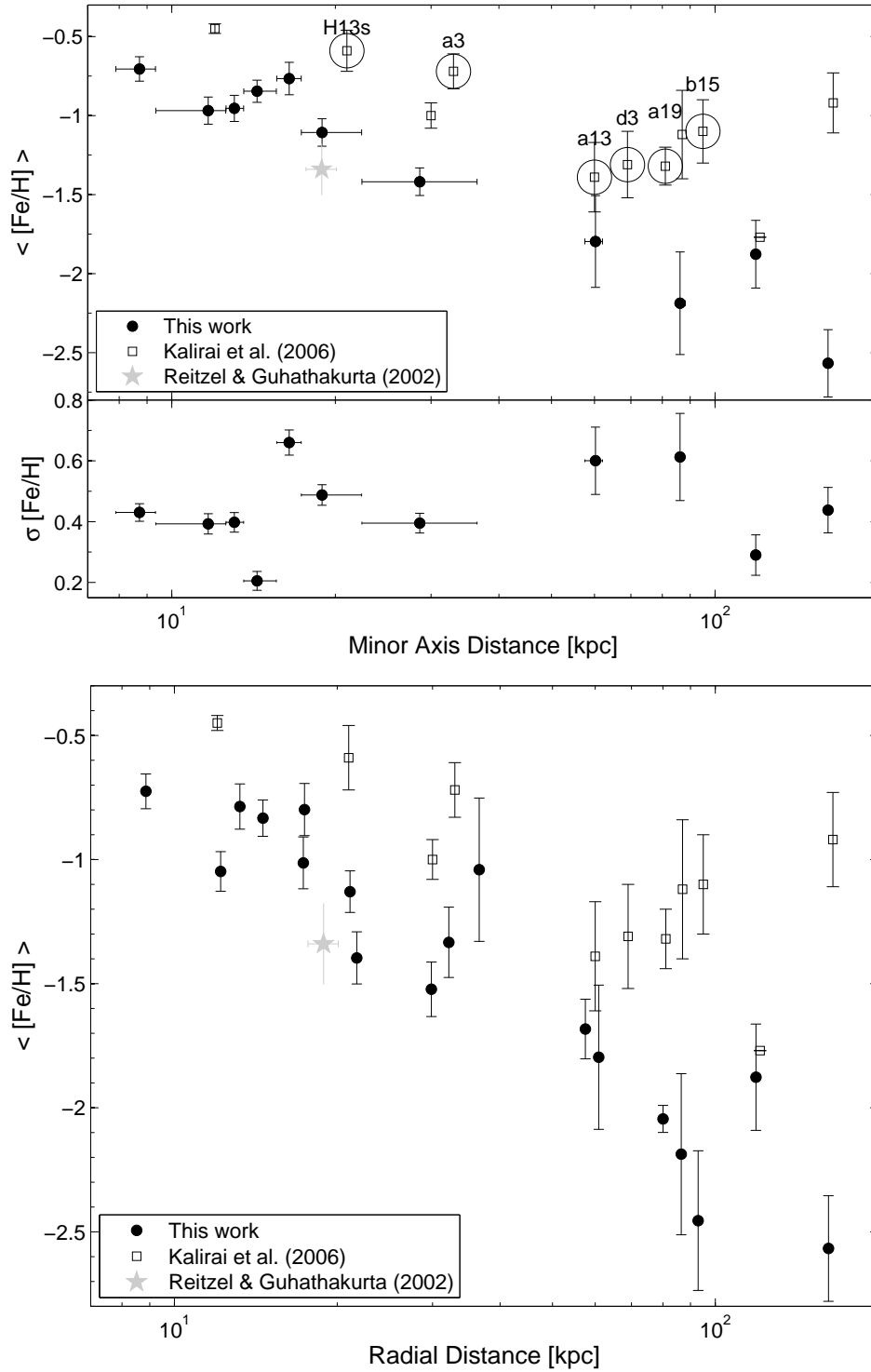


FIG. 16.— Run of mean metallicity and metallicity dispersion as a function of radius. While both our data and those of Kalirai et al. (2006a) show the presence of a gradient, our measurements are more metal poor on average. The top panel only includes our *minor axis* fields with a radial binning to obtain the same number of stars per bin. The points encircled and labelled by their identifier are not located on the minor axis. Horizontal errorbars indicate the extent of our radial binning. The open star indicates the spectroscopic mean  $[Fe/H]$  measurement of Reitzel & Guhathakurta (2002). In the bottom panel, we also include the off-axis fields and compute the mean metallicities separately for each field.



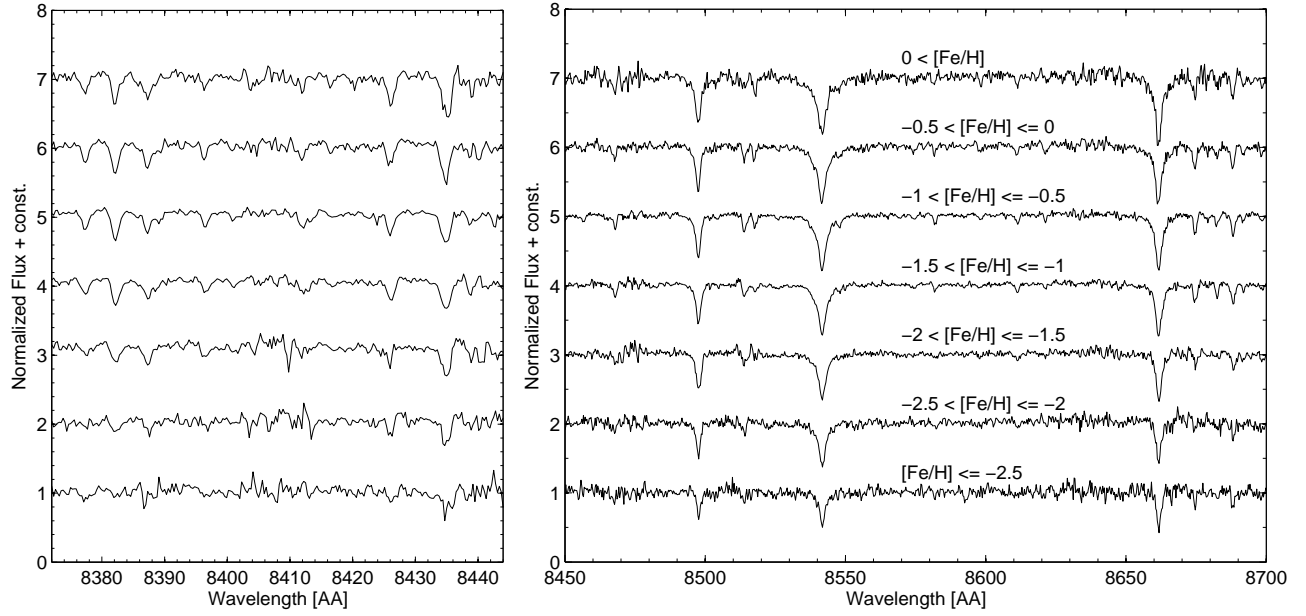


FIG. 17.— Coadded spectra, grouped according to our derived CaT metallicity. Apart from the prominent CaT lines at 8498, 8542, 8662Å (right panel), there are a number of weaker lines (mostly Fe I), which become progressively stronger in the more metal rich spectra (the CaT line strength  $\langle \Sigma W \rangle$  increases from 2.4Å to 7.8Å for the metallicity range covered in this figure). The coaddition also emphasizes a few  $\alpha$ -element lines that become weaker for the more metal poor stars: note for instance the strong Ti I features at 8378, 8426, 8435Å.

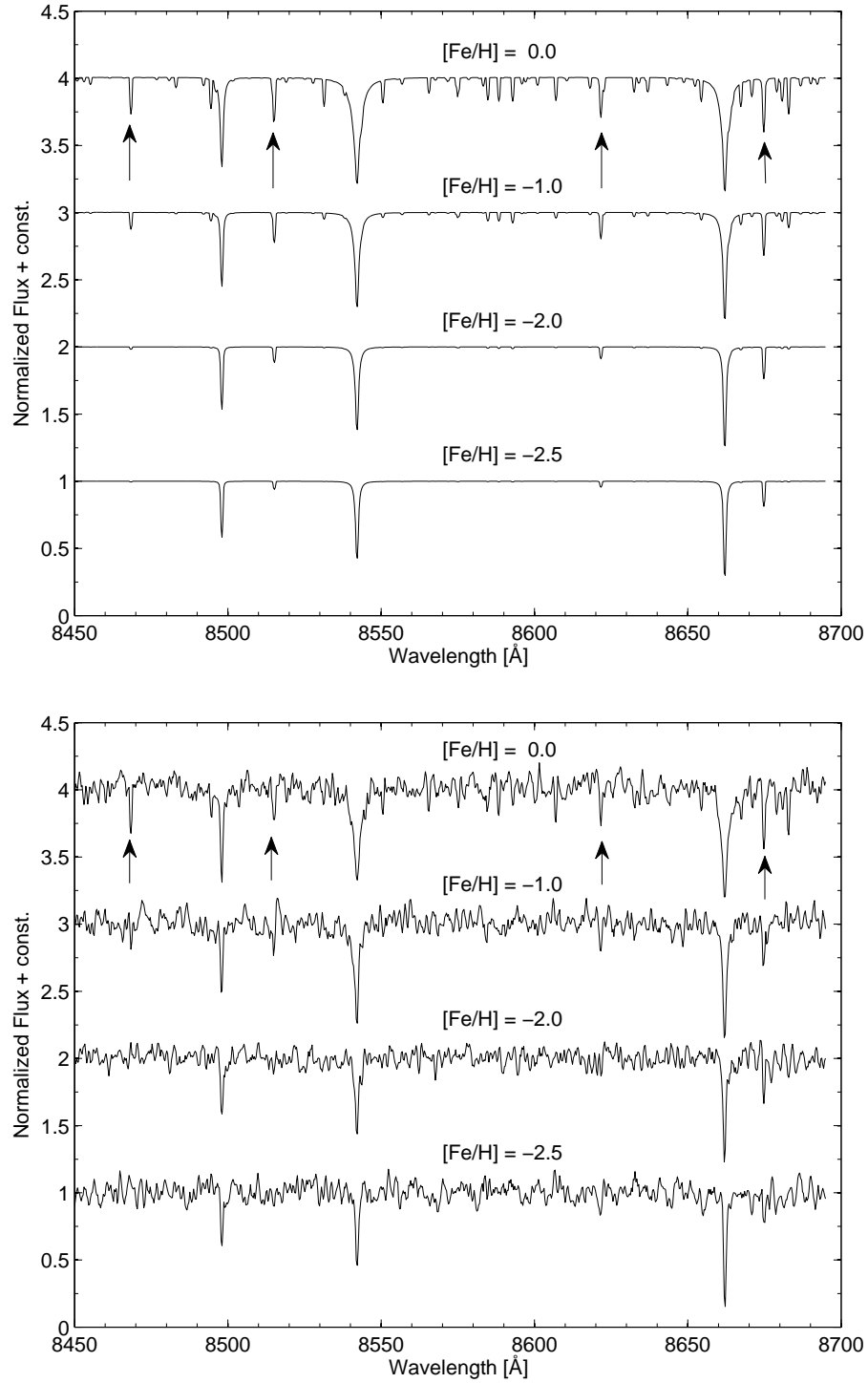


FIG. 18.— Synthetic spectra for a typical red giant, using Kurucz model atmospheres of different metallicities. The spectral resolution was reduced to match that of DEIMOS. Additionally, a noise component was added to the bottom panel to illustrate a  $S/N$  ratio of 10. Even at these low  $S/N$ , visual ranking by the strength of a number iron lines (indicated by arrows) is possible and observable in our spectra (see Fig. 17).

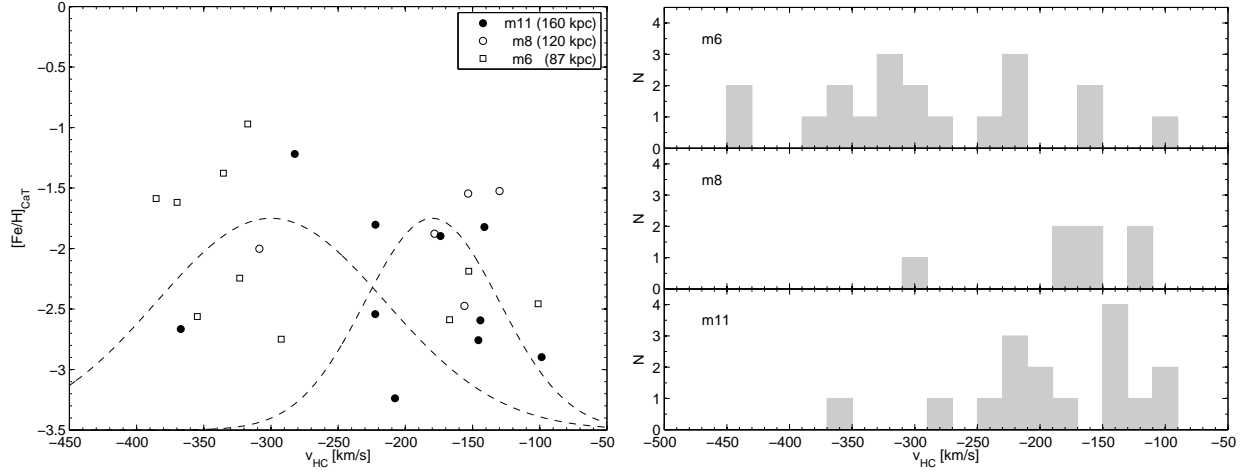


FIG. 19.— Left panel: Metallicity and velocities for giant candidates in the outermost regions  $>40$  kpc (small black dots). Different symbols highlight the distributions in the three outer fields. Also indicated are the velocity number distributions of the M31 halo (at a mean of  $-300$  km s $^{-1}$ ) and that of M33 (around  $-180$  km s $^{-1}$ ) with arbitrary scaling. The right panel shows the respective velocity histograms of these outer stars.

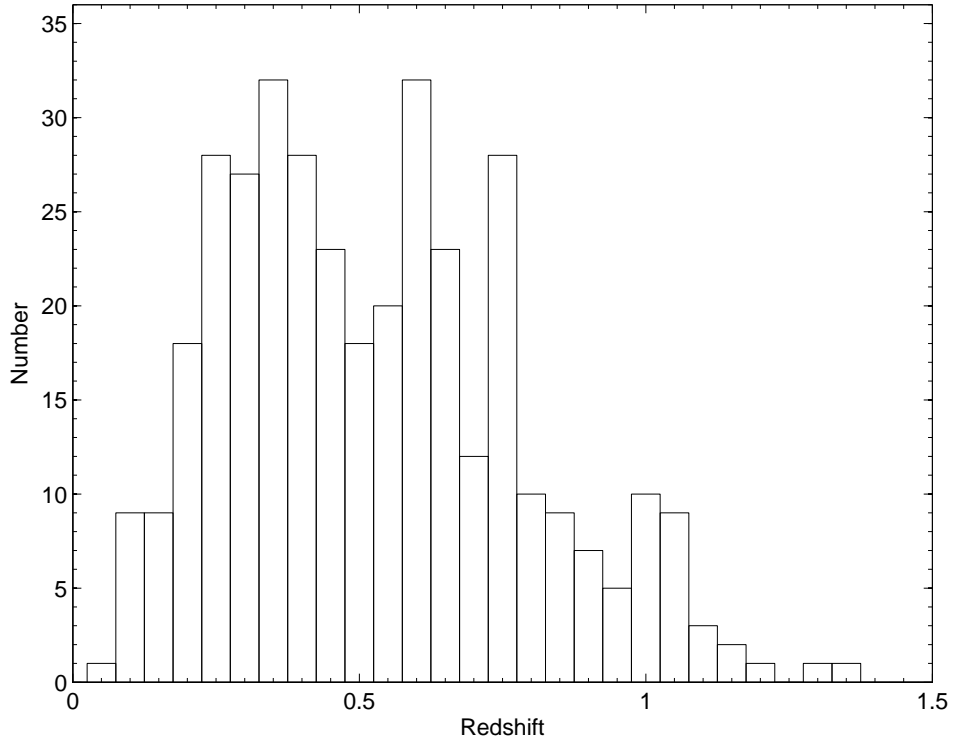


FIG. 20.— Redshift distribution of background galaxies. Their respective color distribution is shown in Fig. 3.